Gravity current flow past a circular cylinder: Forces, wall shear stresses and implications for scour

By E. GONZALEZ-JUEZ[1], E. MEIBURG[1], T. TOKYAY[2] AND G. CONSTANTINESCU[2]

[1]Department of Mechanical Engineering, University of California at Santa Barbara

[2]Department of Civil and Environmental Engineering, University of Iowa

(Received ?? and in revised form ??)

The flow of compositional gravity currents past circular cylinders mounted above a wall is investigated numerically. Two- and three-dimensional Navier-Stokes simulations are employed to quantify the force load on the cylinder, along with the friction velocity at the bottom wall near the cylinder, for Reynolds numbers in the range of $2,000 - 45,000$. While two-dimensional simulations accurately capture the impact stage, they are seen to overpredict the force and friction velocity fluctuations throughout the transient stage. Comparisons between gravity current and constant density flows past circular cylinders show that the impact and transient stages are unique to gravity current flows. During the quasisteady stage, on the other hand, the wake structures and the values of the drag, the peak-to-peak lift, the vortex shedding frequency, and the friction velocity below the cylinder are comparable.

The friction velocity below the cylinder depends chiefly on the Reynolds number formed with the front velocity and the gap width. The maximum friction velocity at impact is about 60% larger than during the quasisteady stage, or in a constant density flow. This raises the possibility of aggressive erosion behavior at impact, which may occur in a spanwise localized fashion due to the larger friction velocity near the lobes.

1. Introduction

As the offshore oil and gas industry moves towards deeper ocean environments, submarine structures such as oil and gas pipelines become increasingly exposed to less understood hazards, among them gravity and turbidity currents (Dengler & Wilde (1987); Niedoroda *et al.* (2000); Ross *et al.* (2004); Bruschi *et al.* (2006)). Such gravity currents form when a heavier fluid propagates into a lighter one in a predominantly horizontal direction (Benjamin (1968); Simpson (1997)). When driven by density differences due to concentration variations of liquids, solutes or gases, these currents are referred to as compositional gravity currents. Alternatively, the driving force may be caused by differential particle loading; in this case the currents are called turbidity currents (Meiburg & Kneller (2009)).

Our incomplete understanding of the interaction between gravity currents and submarine structures in the deep sea has motivated several recent experimental (Ermanyuk & Gavrilov (2005*a*,*b*)) and numerical (Gonzalez-Juez *et al.* (2007, 2008, 2009)) investigations. These indicate that such flows differ fundamentally from the well-studied problem of constant density flows past bluff bodies (Zdravkovich (1997); Williamson (1996)), due

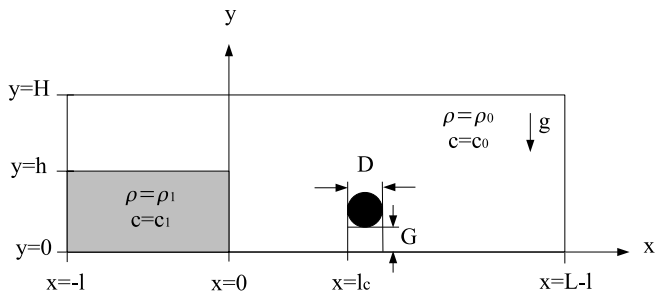

FIGURE 1. Schematic of the flow configuration. A channel of length L and height H contains a lock of length l and height h. When the gate at $x = 0$ is opened, a current of the denser fluid forms and propagates towards a circular cylinder of diameter D, which is situated a distance l_c away from the gate, and a distance G above the bottom wall.

to the presence of a moving front. All of the above studies employ the lock-exchange setup (figure 1), as it allows for the systematic variation of the dominant control parameters. The generic configuration involves a channel of length L and height H, filled with ambient fluid of density ρ_0 and solute concentration c_0. Submerged in it is a lock of length l and height h, which contains a heavier fluid of density ρ_1 and concentration c_1. When the vertical gate at $x = 0$ is opened, the denser fluid forms a compositional gravity current that propagates towards the right along the non-erodible floor of the channel, where it encounters a submerged obstacle after traveling a distance l_c.

Earlier studies based on this configuration have considered both bottom-mounted rectangular cylinders (Ermanyuk & Gavrilov (2005*b*); Gonzalez-Juez *et al.* (2008)), as well as circular cylinders mounted above a wall. For the latter configuration, Ermanyuk & Gavrilov (2005*a*) discuss experimental measurements of the force acting on the cylinder. Corresponding two-dimensional Navier-Stokes simulations by Gonzalez-Juez *et al.* (2009) investigate the relationship between this force and transient flow structures. As will be discussed below, a number of questions are left unanswered by these two-dimensional (2D) calculations, which provides the motivation for the three-dimensional (3D) simulation work to be described here. Nevertheless, the 2D simulations by Gonzalez-Juez *et al.* (2009) are able to reproduce the splitting of the current into a portion that flows beneath the cylinder and creates a jet-like flow, and another portion that flows over the cylinder. Eventually, the current reestablishes itself further downstream. Both experiments and simulations show that the interaction of the gravity current with the cylinder can be divided into an impact, a transient, and a quasisteady stage. During the impact stage, the drag increases exponentially towards a maximum, while the lift undergoes a strong initial fluctuation. The analysis of Gonzalez-Juez *et al.* (2008) shows that the maximum drag at impact can be up to three times as high as during the quasisteady stage. For sufficiently wide gaps and large ratios H/h of the channel and lock heights, the 2D simulations show Karman vortex shedding during the quasisteady stage. The shedding frequency and the *rms*-fluctuations of the lift are close to those for constant density flows past cylinders near walls. However, in contrast to constant density flows, the mean lift now has components due to both buoyancy as well as the slight deflection of the wake by the denser fluid flow. For wide enough gaps and $H/h = 1$, the shear layer between the dense and

light currents is seen to be sufficiently strong and close enough to the cylinder to cancel the roll-up of vorticity, thereby suppressing vortex shedding.

For gravity currents flowing past bottom-mounted square cylinders, Gonzalez-Juez *et al.* (2008) show that 2D and 3D simulations produce nearly identical force profiles during the impact stage. However, 2D simulations can notably overpredict the force fluctuations after impact, as a result of more coherent Kelvin-Helmholtz vortices in two dimensions. We note that for the classical problem of constant density flow past a circular cylinder, Mittal & Balachandar (1995) also found that 2D simulations overpredict the mean drag and *rms*-fluctuations of the lift in comparison with 3D simulations, as vortices are shed closer to the cylinder in 2D simulations. Based on the above observations, our first objective then is to identify the conditions under which results from 2D simulations of gravity current flows past circular cylinders are adequate, and when 3D effects become important (section 3.3). For bottom-mounted square cylinders, the investigation by Gonzalez-Juez *et al.* (2008) sheds some light on the 2D *vs.* 3D issue. However, those results are not directly applicable to the case of a circular cylinder placed some distance above the wall, due to the presence of Karman vortex shedding and the effect of the gap.

The 3D simulations of gravity current flows past bottom-mounted rectangular cylinders by Gonzalez-Juez *et al.* (2008) show that the gravity current's lobe and cleft structure (Simpson (1997)) determines the spanwise variation of the drag at impact. During the quasisteady stage, a cellular flow structure dominates that is similar to the one seen in constant density flows (Martinuzzi & Tropea (1993)). Hence, our second objective is a) to assess the effect of the lobes and clefts on gravity current flows past circular cylinders mounted some distance above a wall, b) to identify the nature of the 3D flow during the quasisteady stage, and c) to discuss the effect of these 3D flow features on the spanwise variation of the drag (section 3.4). In addition, we will compare wake flow structure, mean drag and *rms*-lift fluctuations during the quasisteady stage for gravity current and constant density flows past circular cylinders (sections 3.4 and 3.5). This comparison will provide some guidance as to when the wealth of data for constant density flows past circular cylinders near walls (Bearman & Zdravkovich (1978); Zdravkovich (1985); Fredsøe & Hansen (1987); Chiew (1991); Lei *et al.* (1999, 2000), among many others) is applicable to gravity current flows.

An issue of great concern for flows around pipelines on the seafloor is scour, i.e. the removal of sediment from the vicinity of the pipeline by the flow. Scour represents a threat to the stability of submarine structures, and hence there is great interest in predicting its occurrence. The scour by steady and wavy flows past circular cylinders has been studied extensively in the past (e.g. Whitehouse (1998) and Sumer & Fredsøe (2002)). Similarly, substantial attention has focused on sediment transport by gravity current flows in the absence of obstacles (e.g. the reviews by Middleton (1993), Kneller *et al.* (1999) and Meiburg & Kneller (2009)). However, we are unaware of any fundamental investigations into scour by gravity current flows past cylinders. Hence, our third objective is to take a first step in this direction.

Sumer & Fredsøe (2002) lay out the key mechanisms behind scour. For a circular cylinder situated on an erodible bed, scour starts when the difference in pressure upstream and downstream of the cylinder exceeds a threshold that depends on the properties of the bed. Once this threshold is surpassed, 'piping' sets in and the bed underneath the cylinder is washed away. The simulations to be discussed below will allow us to formulate a criterion for the onset of scour when a gravity current flows over a bottom-mounted cylinder. The onset of scour is followed by aggressive sediment transport below the cylinder, called tunneling erosion, and by somewhat weaker lee-wake erosion downstream of the cylinder.

The total sediment transport rate q_t of the current, in terms of volume of sediment material per unit time and unit width, is composed of a bed load component q_b, and a suspended load component q_s (Graf (1984)). This sediment transport rate q_t has been modeled as a function of the bed properties and the shear stress magnitude $|\tau_w|$ at the bed. It scales as $q_t \sim (|\tau_w| - |\tau_{cr}|)^n$, where $n \geqslant 1$, and $|\tau_{cr}|$ represents a critical wall shear stress. This scaling relationship suggests that the study of sediment transport in gravity current flows past cylinders should begin with the mechanisms that generate the bed shear stresses. Thus our third objective is to quantify the wall shear stresses in gravity current flows past cylinders (section 4). We will first discuss the temporal evolution of $|\tau_w|$ near the cylinder from a representative 3D simulation (section 4.2). It will then be shown that 2D and 3D simulations predict similar values of $|\tau_w|$ near the cylinder at impact and during the quasisteady stage (section 4.3). Based on this finding, we will employ 2D simulations to study the influence of various parameters on the values of $|\tau_w|$ near the cylinder. Finally, we will present qualitative arguments for the evolution of scour in gravity current flows along erodible beds, based on our findings for $|\tau_w|$ in non-erodible beds (section 6).

2. Computational approach

2.1. *Governing equations*

The simulations are based on the Navier-Stokes equations in the Boussinesq approximation, and they follow the approach outlined by Härtel *et al.* (2000*b*) and Ooi *et al.* (2005, 2007*c*,*a*). In the usual way, we introduce the buoyancy velocity

$$u_b = \sqrt{g'h} \ , \tag{2.1}$$

where the reduced gravity g' is defined as

$$g' = g(\rho_1 - \rho_0)/\rho_0 \ . \tag{2.2}$$

The relationship between density and concentration is assumed to be linear

$$\rho = \rho_0 + \frac{\rho_1 - \rho_0}{c_1 - c_0}(c - c_0) \ . \tag{2.3}$$

By introducing suitable characteristic quantities, we can define dimensionless variables as

$$t^* = \frac{t}{(h/u_b)} \ , \ x_i^* = \frac{x_i}{h} \ , \ u_i^* = \frac{u_i}{u_b} \ , \ p^* = \frac{p}{\rho_0 u_b^2} \ , \ c^* = \frac{c - c_0}{c_1 - c_0} \quad . \tag{2.4}$$

As a basis for large-eddy simulations with subgrid scale contributions to the diffusion of momentum and concentration, we thus obtain the governing dimensionless equations for the conservation of mass, momentum and concentration in the form

$$\frac{\partial u_j^*}{\partial x_j^*} = 0 \ , \tag{2.5}$$

$$\frac{\partial u_i^*}{\partial t^*} + \frac{\partial u_i^* u_j^*}{\partial x_j^*} = -\frac{\partial p^*}{\partial x_i^*} + \frac{\partial}{\partial x_j^*}\left(\left(\frac{1}{Re} + \nu_{SGS}^*\right)\left(\frac{\partial u_i^*}{\partial x_j^*} + \frac{\partial u_j^*}{\partial x_i^*}\right)\right) + c^* \, e_i^g \ , \tag{2.6}$$

$$\frac{\partial c^*}{\partial t^*} + \frac{\partial c^* u_j^*}{\partial x_j^*} = \frac{\partial}{\partial x_j^*}\left(\left(\frac{1}{Re\,Sc} + \kappa_{SGS}^*\right)\frac{\partial c^*}{\partial x_j^*}\right) . \tag{2.7}$$

Here u_i^* denotes the velocity vector, p^* the total pressure, c^* the concentration, and e_i^g indicates the unit vector pointing in the direction of gravity. The spatial coordinates are denoted alternatively by (x, y, z) or by (x_1, x_2, x_3). As governing dimensionless parameters in equations (2.5)-(2.7) we identify the Reynolds and Schmidt numbers, respectively,

$$Re = \frac{u_b h}{\nu} , \; Sc = \frac{\nu}{\kappa} , \tag{2.8}$$

where ν represents the kinematic viscosity and κ the molecular diffusivity. A Reynolds number based on the cylinder diameter D and the velocity U to which the cylinder is exposed (to be defined later) is also used throughout the present work, and is given by $Re_D = UD/\nu$. In addition, there are various geometrical parameters, the most important ones being H/h, D/h, and G/h.

We remark that in the following discussion, it will generally be advantageous to render time dimensionless by means of the front velocity V of the gravity current, since this will frequently lead to a better collapse of data from different flow fields (Gonzalez-Juez *et al.* (2008)). Nevertheless, in deriving the above equations we employ u_b for nondimensionalizing time, since this quantity is known *a priori*, whereas V can be determined only in the course of carrying out the numerical experiment. For the same reason, the lock height h is taken as the length-scale, rather than the gravity current height. We note that the height of lock-exchange currents usually is close to $h/2$ (Shin *et al.* (2004)).

In the 2D simulations, all of the scales of motion are resolved by choosing a sufficiently fine grid, and by setting the subgrid viscosity ν_{SGS}^* and diffusivity κ_{SGS}^* in equations (2.6) and (2.7) to zero. On the other hand, the 3D simulations employ a large-eddy simulation (LES) approach, so that a higher Reynolds number regime can be reached. With the LES approach, only the large energy-containing scales are resolved, while the effect of the small unresolved scales on the large scales is modeled by evaluating ν_{SGS}^* and κ_{SGS}^* in equations (2.6) and (2.7) with the dynamic Smagorinsky model (Germano *et al.* (1991), Lilly (1992)). Additional details are provided in Ooi *et al.* (2007*a*) and Pierce (2001).

Unless otherwise stated, the bottom ($y = 0$) and left ($x = -l$) boundaries of the computational domain, and the surface of the cylinder, are treated as no-slip walls. The top boundary ($y = H$) is considered to be a slip wall. A convective boundary condition is employed along the right boundary ($x = L - l$) of the domain (Pierce (2001)). In the 3D simulations, the flow in the spanwise z-direction is assumed to be periodic. The flow field is initialized with the fluid at rest everywhere, and the dimensionless concentration c^* being one (zero) within (outside) the lock.

2.2. *Numerical methodology*

Equations (2.6)-(2.7) are discretized on a non-equidistant Cartesian mesh and solved with a finite-volume DNS/LES code (Pierce (2001), Pierce & Moin (2004)). The simulation of irregular domains is accomplished by means of a grid blanking methodology. The velocity components are represented in a staggered fashion with respect to pressure and concentration, in both space and time. All differential operators are discretized using central differences, except for the convection term in the concentration conservation equation (2.7), which is discretized using the QUICK scheme. Time integration is accomplished via an iterative procedure similar to the Crank-Nicolson scheme. To ensure that

	$Re_D = 250$		$Re_D = 525$	
parameter	Posdziech & Grundmann (2007)	our results	Mittal & Balachandar (1995)	our results
$F_{D,mean}/(0.5\rho_0 DU^2)$	1.33	1.31	1.44	1.36
$F_{L,pp}/(0.5\rho_0 DU^2)$	1.60	1.62	2.42	2.30
$f/(U/D)$	0.202	0.205	0.210[1]	0.215
L_w/D			0.50	0.50
first separation point			112^o	110^o
second separation point			137^o	138^o

TABLE 1. Comparison of results from our simulations and those of others for constant density flows past circular cylinders at $Re_D = 250$ and $Re_D = 525$. The quantities considered are: the mean drag $F_{D,mean}/(0.5\rho_0 DU^2)$, peak-to-peak lift $F_{L,pp}/(0.5\rho_0 DU^2)$, vortex shedding frequency $f/(U/D)$, and wake length (L_w/D). Also shown are the location of the first and second separation points behind the cylinder, which can be seen in the mean streamline plots of figure 12 in Mittal & Balachandar (1995); for reference, the stagnation point is at 0^o, the top of the cylinder at 90^o, and the base at 180^o. ([1] This value is from the experiments by Prasad & Williamson (1997) at $Re_D = 592$.)

the continuity equation (2.5) is satisfied, a Poisson equation for the pressure correction is solved at each time step by means of a multigrid algorithm. The numerical method is second order accurate in both space and time.

Our code has been validated for the simulation of intrusion currents (Ooi *et al.* (2007*b*)), gravity currents over no-slip walls (Ooi *et al.* (2005, 2007*a*,*c*)), and gravity current flows past bottom-mounted square cylinders (Gonzalez-Juez *et al.* (2007, 2008)), as well as for the simulation of flows past open cavities in which a passive or active scalar is present (Chang *et al.* (2006, 2007*a*,*b*)), and other types of flows (Pierce (2001), Pierce & Moin (2004)). In addition, the predictions of our code for the mean drag, peak-to-peak lift, and vortex shedding frequency in 2D flows past square cylinders inside channels are in good agreement with those from recent codes (Gonzalez-Juez & Meiburg (2009)).

Since in the present simulation work the circular cylinder is approximated in a cartesian mesh, we present additional validation data comparing our results with those from other computational investigations of 2D constant density flows past circular cylinders. The two values of $Re_D = UD/\nu$ considered are 250 and 525, where U is the free stream velocity. The complete parameters of these 2D simulations can be found in Gonzalez-Juez (2009). Table 1 shows that at $Re_D = 525$ ($Re_D = 250$) the mean drag calculated with our code is within 6% (2%), the vortex shedding frequency is within 2% (1%), and the peak-to-peak lift is within 5% (1%). The level of agreement between our results and those from other investigations is satisfactory for the objectives of the present work. This agreement reflects the fact that the boundary layer on the cylinder is sufficiently thick for the surface roughness not to have a strong influence for the values of Re_D considered here.

2.3. *Parameter range of the simulations*

The length of the computational domain is kept at $L/h = 28$ for all simulations, and its width in the spanwise direction is equal to h for the 3D simulations. The constant lock length of $l/h = 12$ ensures that, during the time of the simulation, reflections from the left wall do not influence the interaction between the gravity current front and the cylinder, so that a constant flux of dense fluid towards the cylinder is maintained. The

l_c/h	9	3	3	9
Re	9,000	9,000	9,000	45,000
G/h	0.03	0.03	0.15	0.03

TABLE 2. Parameter values employed in the 3D simulations.

ratio of the channel height and the lock height is set to $H/h = 2.5$, which approximates well the deep ambient case of $H/h \to \infty$ found in practice (Gonzalez-Juez *et al.* (2008)). The distance between the gate and the cylinder is set to $l_c/h = 3$ for most simulations, since it ensures that the current is in the constant front speed phase (Simpson (1997)) when it encounters the cylinder. However, whereas a value of $l_c/h = 3$ is large enough for l_c/h not to be an important parameter of the problem in 2D simulations (Gonzalez-Juez *et al.* (2008)), we will see that larger values are needed in 3D simulations; thus, we also consider a value of $l_c/h = 9$ in 3D simulations. Reynolds numbers in the range $Re = 2,000 - 45,000$ are considered, which are typical of laboratory gravity currents. The Schmidt number Sc has a small effect on the dynamics of the flow and is kept at unity (Gonzalez-Juez *et al.* (2008)). The ratio of the cylinder diameter and the lock height is $D/h = 0.1$. For comparison, typical gravity current heights of O(1-100m) and cylinder length scales of $O(1m)$ yield a range of $D/h = 0.005 - 0.5$. A range of gap widths of $G/h = 0.015 - 0.15$ ($G/D = 0.15 - 1.5$) is explored, which corresponds to values typically generated through scouring (e.g. Sumer & Fredsøe (2002)).

A grid of 1,600×320×60 (1,600×320) is employed in the 3D (2D) simulations. The grid is refined near the cylinder to ensure a streamwise and vertical grid spacing of $0.01D$ there. In addition, the grid is also refined near the bottom wall, where the vertical grid spacing is of the order of $0.001h$. With this grid refinement near the wall, the value of the eddy viscosity ν^*_{SGS} at this location is two (one) orders of magnitude less than $1/Re$ in the simulations at $Re = 9,000$ ($Re = 45,000$). The time step size is limited such as to keep the CFL number below a suitable value determined in test simulations. Grid resolution tests were conducted by comparing results from 2D simulations with grids of 800×160, $1,600 \times 320$, and $2,400 \times 520$. Because the results for a grid of $1,600 \times 320$ were found to be in good agreement with those for $2,400 \times 520$, the former discretization was selected. For example, the maximum drag at impact, the amplitude of the initial fluctuation of the lift, and the maximum wall shear stress right below the cylinder at impact agreed to within less than 1% for these two grids.

The parameter combinations of the 3D simulations are shown in table 2, and those of further simulations will be discussed later.

3. Force acting on the cylinder

3.1. *Reference case*

The parameters for the reference 3D simulation are $Re = 9,000$, $l_c/h = 9$, $D/h = 0.1$, and $G/h = 0.03$; the Reynolds number based on the cylinder's diameter is $Re_D = 459$, as discussed in section 3.5. Figures 2(a-c) show the temporal evolution of the flowfield for the reference case by means of spanwise vorticity isosurfaces, which highlight the interface between the fluids. The cylinder's center is located at $x/h = 9.05$ for the reference case. Notice in figure 2a the lobe and cleft structure at the current front (Simpson (1972)), as well as the Kelvin-Helmholtz billows further upstream. In figure 2b, the gravity current front has just encountered the cylinder, and is now plunging downward immediately

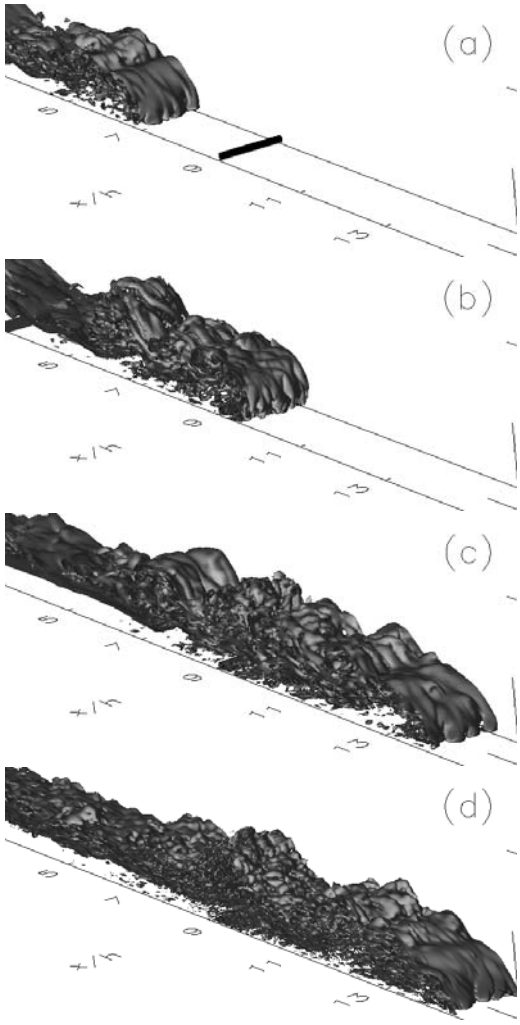

FIGURE 2. Temporal evolution of the gravity current for $Re = 9,000$ (a-c) and $Re = 45,000$ (d). Other parameter values are $D/h = 0.1$, $l_c/h = 9$, and $G/h = 0.03$. Instantaneous spanwise vorticity isosurfaces ($\omega_z/(V/h) = 1$) are shown at $t/(h/V) = 7.1$ (a), 10 (b), 14.8 (c), and 14.6 (d).

downstream of the cylinder. Later on, the current reestablishes itself downstream of the cylinder, cf. figure 2c.

Figures 3 and 4a allow us to associate the temporal evolution of the flowfield with the instantaneous force components acting on the cylinder, and to define the three stages of the interaction. Here the force exerted by the fluid on the cylinder is calculated by integrating the total pressure around the circumference of the cylinder. The contribution from the shear stresses around the cylinder is negligible for the range of parameters considered (Gonzalez-Juez *et al.* (2007, 2008, 2009)). The x- and y-components of the force are referred to as drag F_D and lift F_L, respectively. They are scaled as $F_D/(0.5\rho_0 DV^2)$ and $F_L/(0.5\rho_0 DV^2)$, while time is normalized as $t/(h/V)$ (Gonzalez-Juez *et al.* (2008)). The front speed V of the gravity current is calculated by tracking the foremost point of the $c^* = 0.5$ concentration isosurface. Before the current meets the cylinder, its front speed has a value of $V/u_b = 0.59$ for the reference case ($H/h = 2.5$ and $Re = 9,000$). This

value compares well with the experimental data of $V/u_b = 0.57$ ($V/u_b = 0.60$) obtained by Shin *et al.* (2004) for $H/h = 2$ ($H/h = 3$).

The drag increases exponentially as the gravity current approaches the cylinder, cf. figure 3a, and it reaches a maximum at $t/(h/V) = 9.2$ when the current meets the cylinder, cf. figure 3b, marking the end of what we define here as the impact stage. During this stage the lift undergoes a strong initial fluctuation, cf. figure 4a. Notice the formation of a jet of dense fluid in the gap (figure 3b,c) and the later plunge of the head of the current downstream of the cylinder in figure 3d. These two processes are associated with high levels of shear stresses at the bottom wall, as will be seen in section 4. After impact, the drag and lift undergo fluctuations during the transient stage, which ends once these quantities reach a mean quasisteady value by $t/(h/V) \approx 18$; the so-called quasisteady stage then begins.

3.2. *High Reynolds number case*

A comparison between the reference case ($Re = 9,000$, $l_c/h = 9$, and $G/h = 0.03$) and the $Re = 45,000$ case reveals two important differences. First, note that the spanwise vorticity in the mixing layer between the two fluids and in the cylinder wake takes the form of larger scale, coherent patches in the reference case, cf. figures 2c and 3e,f. On the other hand, these patches are of a much smaller scale, and much more intermittent, in the $Re = 45,000$ case, cf. figures 2d and 5. This suggests, from a qualitative standpoint, that these flow regions appear to be laminar or at most weakly turbulent in the reference case, and turbulent for $Re = 45,000$. The second important difference between these two cases concerns the stronger initial lift fluctuations in the interval $t/(h/V) = 9-11$ for the lower Re case, cf. figures 4a and 4b. A key mechanism for generating these fluctuations is the temporal variation of the horizontal velocity difference between locations right above the cylinder, outside the boundary layer, and the gap (Gonzalez-Juez *et al.* (2007, 2009)). This horizontal velocity difference, which can be related to the lift through Bernoulli's principle, is larger for the lower Re case, resulting in stronger lift fluctuations.

3.3. *Range of validity of 2D simulations*

Earlier investigations of gravity current flows without submerged cylinders observed the formation and convection of separated flow structures along the bottom wall by the action of the Kelvin-Helmholtz billows at the interface between the two fluids (Härtel *et al.* (2000*b*); Cantero *et al.* (2007)). Our recent simulations of gravity current flows past bottom-mounted square cylinders show that these Kelvin-Helmholtz billows and separated structures affect the unsteady force loads after impact (Gonzalez-Juez *et al.* (2008)). This effect is more pronounced in 2D than in 3D simulations, since these flow structures are more intense and coherent in 2D simulations. Furthermore, while the effect of these flow structures on the unsteady force load is limited to the transient stage in 3D simulations, it can last much longer in 2D simulations at higher Reynolds numbers of $O(10,000)$, as the 3D break-up due to spanwise instabilities is absent in 2D simulations (Gonzalez-Juez *et al.* (2008)). Consequently, the force fluctuations beyond the impact stage are notably overpredicted by 2D simulations at large Re-values. Below we will find that for circular cylinders with a gap, even in 2D simulations the effect of these separated structures on the unsteady force load is limited to the transient stage. This represents a key difference between the cases of a circular cylinder with a gap and a bottom-mounted rectangular cylinder, respectively.

We begin by focusing on the influence of the distance l_c/h between the gate and the cylinder on the temporal evolution of the flowfield and the force loads in 3D simulations. This will be helpful for interpreting the subsequent comparison of 2D and 3D simulation

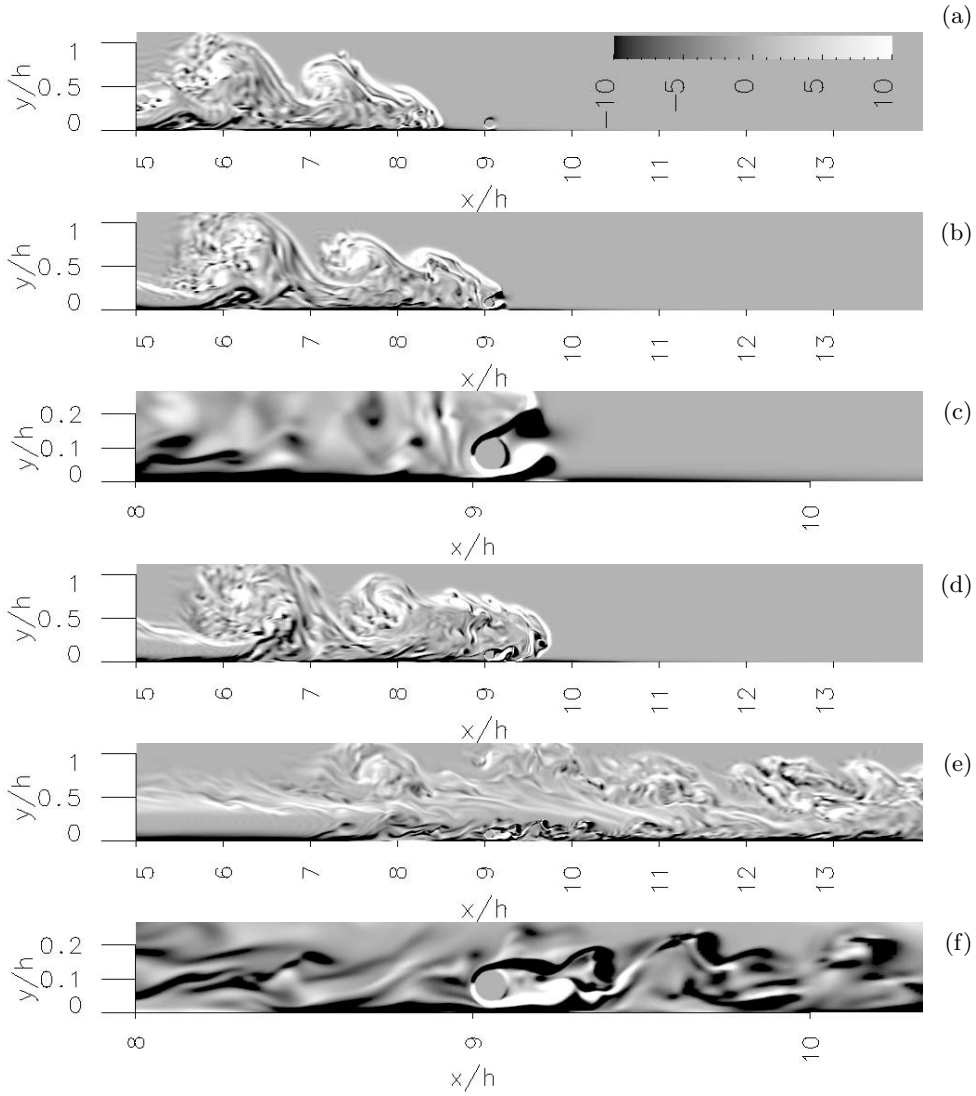

FIGURE 3. Spanwise vorticity $\omega_z/(V/h)$ fields at $z/h = 0.5$ and different times for the reference case $Re = 9,000$, $D/h = 0.1$, $l_c/h = 9$, and $G/h = 0.03$: (a) $t/(h/V) = 8.5$, (b,c) $t/(h/V) = 9.2$, (d) $t/(h/V) = 9.9$, and (e,f) $t/(h/V) = 16.3$. The cylinder is located at $x/h = 9 - 9.1$. The region near the cylinder in frames (b) and (e) is enlarged in frames (c) and (f), respectively. Note the formation of a jet of dense fluid in the gap in frames (b,c), and the later plunge of the current downstream of the cylinder in frame (d). These two processes are associated with high levels of shear stresses at the bottom wall, cf. section 4.

results. For the reference case with $l_c/h = 9$, the cylinder is located sufficiently far from the gate to allow for the 3D breakup of the Kelvin-Helmholtz billows and their associated recirculation zones along the bottom wall before the current meets the cylinder, cf. figures 3a, 3e, and 3f. On the other hand, for $l_c/h = 3$, the cylinder is too close to the gate to allow for this breakup, and hence the resulting Kelvin-Helmholtz billows and recirculation zones are still very coherent by the time they encounter the cylinder, cf. figures 6a and b. Consequently, as figure 7 shows, while the drag undergoes only one large fluctuation in the time interval $3.3 < t/(h/V) < 14$ for the reference case with $l_c/h = 9$, it undergoes

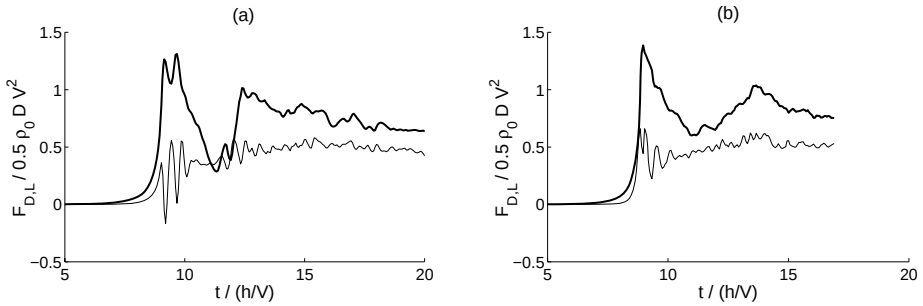

FIGURE 4. Temporal evolution of the spanwise-averaged drag (thick lines) and lift (thin lines) for $Re = 9,000$ (a) and $Re = 45,000$ (b). Other parameter values are $D/h = 0.1$, $l_c/h = 9$, and $G/h = 0.03$. The lift fluctuation during the impact stage is lower for the higher Reynolds number case.

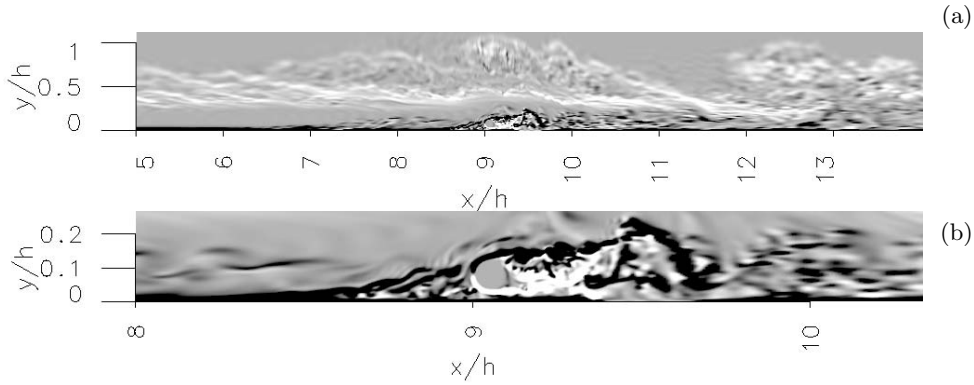

FIGURE 5. Spanwise vorticity $\omega_z/(V/h)$ field at $z/h = 0.5$ and $t/(h/V) = 16.9$ for $Re = 45,000$, $D/h = 0.1$, $l_c/h = 9$, and $G/h = 0.03$. The cylinder is located at $x/h = 9 - 9.1$. The region near the cylinder is enlarged in frame (b).

three large fluctuations in the same time interval for the case with $l_c/h = 3$. Note that the curve for the reference case has been shifted along the abscissa in figure 7 in order to have the first drag maxima of both cases coincide. The maximum drag at impact is affected only weakly by this change of l_c/h ($< 10\%$ change). We can conclude that, as long as l_c/h is sufficiently large for the current to reach a constant front velocity and to allow for the 3D break-up of the Kelvin-Helmholtz billows, this quantity is no longer a dominant parameter.

For the sake of completeness we mention that corresponding 2D simulations (not shown here) show the effect of l_c/h on the force fluctuations during the transient stage to be much less pronounced, as long as the current front has reached a constant velocity by the time it encounters the cylinder.

We now focus on comparing predictions from 2D and 3D simulations for two values of the gap (G/h). For a detailed discussion of the effect of the gap size in 2D simulations, the reader is referred to Gonzalez-Juez *et al.* (2009). For the impact stage $t/(h/V) < 3.3$, figure 8 shows the 2D and 3D simulation results to be in good agreement. For the quasisteady stage $t/(h/V) > 14$, on the other hand, the amplitude of the force fluctuations is overpredicted by the 2D simulations, while their frequency is accurately captured. Note that the increase of the fluctuation amplitude with G/h is reproduced correctly by the 2D simulations. During this late stage, both 2D and 3D simulations show

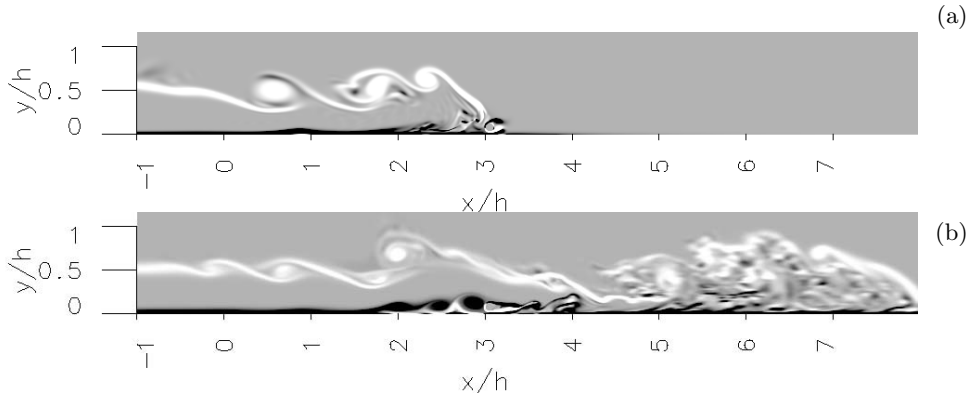

FIGURE 6. Spanwise vorticity $\omega_z/(V/h)$ fields at $z/h = 0.5$ and at different times for $Re = 9,000$, $D/h = 0.1$, $l_c/h = 3$, and $G/h = 0.03$. (a) $t/(h/V) = 3.2$, and (b) $t/(h/V) = 8.3$. The cylinder is located at $x/h = 3 - 3.1$, which is too close to the gate to allow for the 3D breakup of the Kelvin-Helmholtz billows. This results in large force fluctuations during the transient stage.

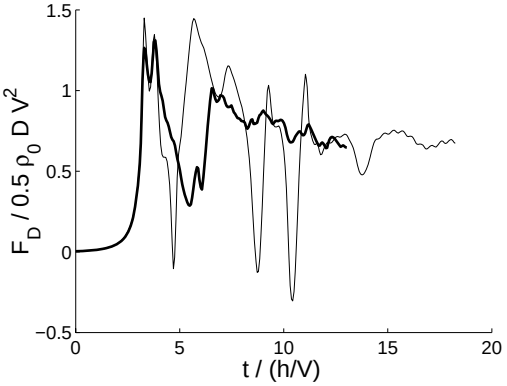

FIGURE 7. Temporal evolution of the spanwise-averaged drag for the reference case $Re = 9,000$, $D/h = 0.1$, $l_c/h = 9$, and $G/h = 0.03$ (thick solid line), and for the case with the same parameters but a shorter distance $l_c/h = 3$ between the gate and the cylinder (thin solid line). The curve for the reference case has been shifted along the abscissa so that the first drag maxima of both cases coincide.

the presence of Karman vortex shedding for the larger gap, cf. figure 9 for 3D results. Conversely, for the smaller gap only clockwise vortices exist (figure 3), since the vorticity in the cylinder's bottom shear layer is effectively canceled by the vorticity of opposing sign in the bottom wall boundary layer (Taniguchi & Miyakoshi (1990); Lei *et al.* (2000); Gonzalez-Juez *et al.* (2009)). Neither 2D nor 3D simulations show the convection of separated flow structures along the bottom wall upstream of the cylinder during the quasisteady stage, for the present parameters. Hence the observed overprediction of the force fluctuations during the quasisteady stage by 2D simulations is not due to overly coherent recirculation regions along the bottom wall. Rather, they occur for the same reason as in constant density flows, i.e., by the shedding of vortices closer to the cylinder in 2D simulations (Mittal & Balachandar (1995)).

During the transient stage ($t/(h/V) = 3.3 - 14$), figure 8 shows that 2D simulations significantly overpredict the amplitude of the force fluctuations, especially for the larger gap. This overprediction is caused by the more coherent Kelvin-Helmholtz billows in the 2D simulations. Figures 8b and 8d appear to suggest that 2D simulations can capture

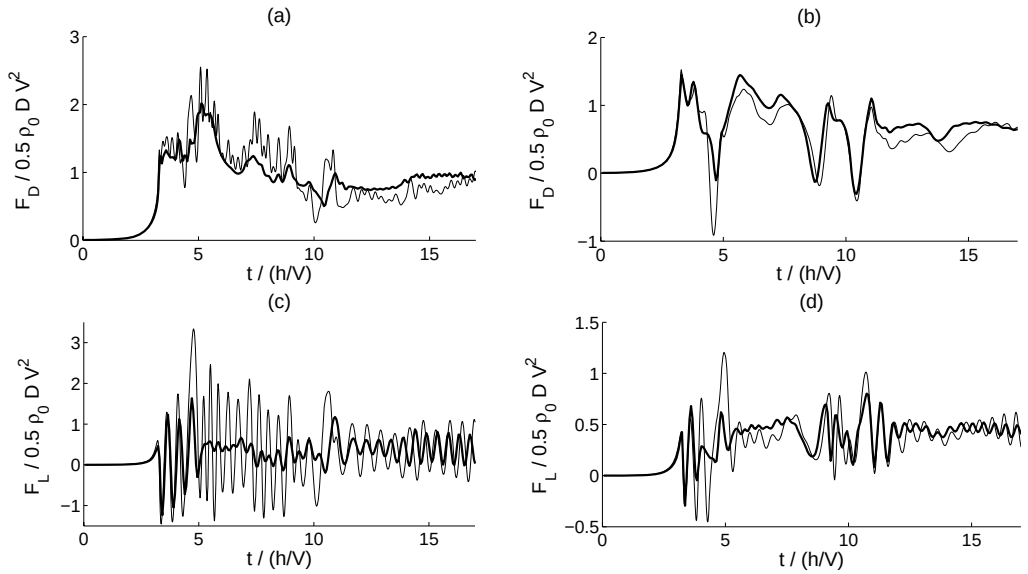

FIGURE 8. Comparison of the spanwise-averaged drag (a,b) and lift (c,d) between 2D (thin lines) and 3D (thick lines) simulations for $Re = 9,000$, $D/h = 0.1$, $l_c/h = 3$, and $G/h = 0.15$ (a,c) and $G/h = 0.03$ (b,d). 2D simulations of gravity current flows past circular cylinders provide quantitatively accurate information for the impact stage. During the later flow stages, they capture the correct fluctuation frequency, while overpredicting the fluctuation amplitude.

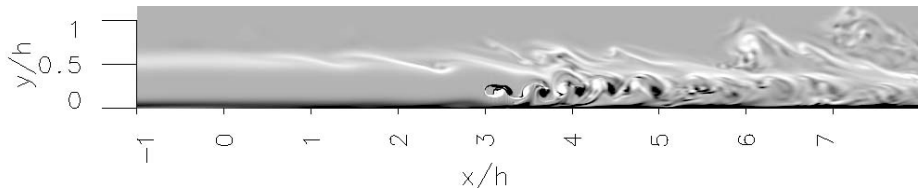

FIGURE 9. Spanwise vorticity $\omega/(V/h)$ field at $z/h = 0.5$ and at $t/(h/V) = 16.5$ for $Re = 9,000$, $D/h = 0.1$, $l_c/h = 3$, and $G/h = 0.15$. The cylinder is located at $x/h = 3 - 3.1$. Notice the presence of Karman vortex shedding for sufficiently large values of G/h.

the force fluctuations for the smaller G/h quite accurately, with the exception of the interval $t/(h/V) = 4 - 6$. However, this good agreement is just coincidental: the value of l_c/h selected for the 3D simulation is too small to allow for the break-up of the Kelvin-Helmholtz billows. When comparing the 2D results with the 3D reference case in figure 7, we notice a substantial discrepancy.

To summarize, 2D simulations of gravity current flows past circular cylinders can be employed to obtain quantitative information for the impact stage. During the later stages, they correctly predict the dominant fluctuation frequency, while overpredicting the fluctuation amplitude. This supports the 2D results for gravity current flows with $H/h = 5$ and $Re = 2,000$ and $6,000$ discussed in Gonzalez-Juez *et al.* (2009). These conclusions are similar to those reached earlier for bottom-mounted square cylinders (Gonzalez-Juez *et al.* (2008)), even though they address a fundamentally different flow configuration with strong force fluctuations due to vortex shedding.

3.4. *Spanwise variation of the drag and associated flow structures*

3.4.1. *Impact stage*

Figure 10a shows a spanwise peak-to-peak variation of the drag of up to 30% during impact. The following discussion provides evidence that this spanwise variation is governed by the gravity current's frontal lobe and cleft structure. Right after the gate at $x = 0$ is opened (figure 1), a filamentary flow structure forms at the front of the current (Härtel *et al.* (2000*b*,*a*)) and later develops into the lobe and cleft structure (Simpson (1972)), cf. also figure 2a. The temporal evolution of this lobe and cleft structure before impact is visualized in figure 10b by means of concentration $c^* = 0.1$ isolines in the $y/h = 0.002$ plane.

Figure 10 shows that the lobes hit the cylinder at approximately $z/h = 0.16$, 0.42, and 0.77, and that the drag reaches instantaneous peaks at these locations during the impact stage. The other 3D simulations conducted within this investigation display similar behavior, as do earlier simulations for bottom-mounted square cylinders (Gonzalez-Juez *et al.* (2008)). This suggests that the spanwise drag variation at impact is determined by the gravity current's lobe and cleft structure, even when a gap exists between the cylinder and the bottom wall. We remark that in the 3D simulations with $l_c/h = 3$, even though the Kelvin-Helmholtz billows do not break up before the current meets the cylinder, a developed lobe and cleft structure is observed. An increase of the Reynolds number, from $Re = 9,000$ in the reference case to $Re = 45,000$, produces a somewhat smaller characteristic spanwise length scale of the drag variation, cf. figure 11, which results from smaller lobe sizes at higher values of Re (from data not shown here and from Simpson (1972)). A spanwise drag variation governed by the lobe and cleft structure is also observed when the gap is increased, from $G/h = 0.03$ in the reference case to $G/h = 0.15$.

3.4.2. *Quasisteady stage*

Figure 12 shows the spanwise variation of the drag at different times during the quasisteady stage, as well as the drag value averaged during the interval $14.2 < t/(h/V) < 17.7$, for the simulations with $Re = 9,000$, $l_c/h = 3$ and $G/h = 0.03$ and 0.15, respectively. The drag variation exhibits a characteristic length scale on the order of D, which is especially noticeable in the large gap case. We remark that during the quasisteady stage the lobe and cleft structure is not longer present.

For the larger gap case ($G/h = 0.15$), figure 13 shows the presence of primary von Karman vortices, cf. also figure 9, and of secondary streamwise vortices in the near wake. These flow structures are similar to those seen in the classic problem of constant density flow past a circular cylinder at Re_D values of a few hundred (Williamson (1996)). We remark that $Re_D = UD/\nu = 459$ for the reference case, as discussed in section 3.5. The spacing of the streamwise vortices scales with D, cf. figure 13 for the gravity current flow and figure 14 in Williamson (1996) for the classic flow. Hence we can conclude that these vortices cause the D-scale spanwise drag variation in figure 12a. Figures 13 and 14 show that a decrease of the gap considerably distorts the flow structures in the near wake, which explains the suppression of the D-scale spanwise drag variation in figures 12c.

3.5. *Comparison with the classic flow past a circular cylinder*

For sufficiently large gaps, the above discussion indicates strong similarities between the quasisteady wake flow structures and the classic constant density flow past a circular cylinder. We will now quantify this level of agreement for $Re = 9,000$, $l_c/h = 3$ and $G/h = 0.15$ by focusing on the mean drag, the peak-to-peak lift variation, and the frequency of the force fluctuations, cf. the data in table 3.

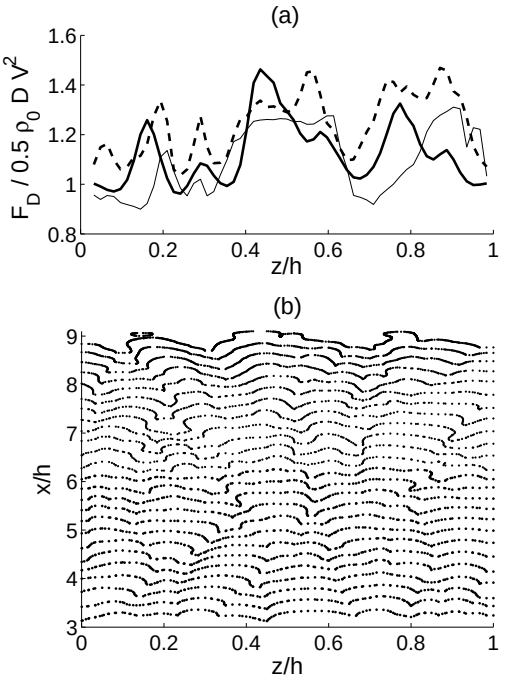

FIGURE 10. (a) Spanwise variation of the drag for $Re = 9,000$, $D/h = 0.1$, $l_c/h = 9$ and $G/h = 0.03$ at different times during the impact stage: $t/(h/V) = 9.1$ (thick solid line), 9.2 (dashed line), and 9.3 (thin solid line). (b) Temporal evolution of the lobe and cleft structure before impact, visualized by concentration $c^* = 0.1$ isolines in the $y/h = 0.002$ plane during the interval $3.5 < t/(h/V) < 9.2$. The cylinder is located at $x/h = 9 - 9.1$. The spanwise drag variation at impact is determined by the gravity current's lobe and cleft structure.

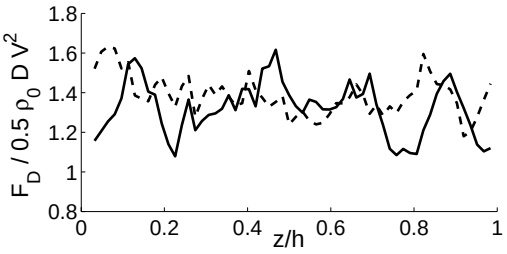

FIGURE 11. Spanwise variation of the drag for $Re = 45,000$, $D/h = 0.1$, $l_c/h = 9$ and $G/h = 0.03$ at $t/(h/V) = 8.6$ (solid line) and 8.7 (dashed line) during impact.

For the gravity current flow, the effective free stream velocity U is approximately constant during the quasisteady stage, at a value $U = 0.86V$, cf. figure 15. This agrees with the finding by Thomas *et al.* (2003) that the fluid velocity within the gravity current some distance upstream of the head is lower than at the head itself. The Reynolds number $Re_D = UD/\nu$ based on U and the cylinder diameter thus has a value of 459, which is sufficiently close to the values investigated by Mittal & Balachandar (1995) and Prasad & Williamson (1997) to make a valid comparison. As Zdravkovich (1997) demonstrates, in this range of Reynolds numbers the quantities of interest depend only weakly on Re. The quantities shown in table 3 are calculated from 8 shedding cycles during the quasisteady stage $14.2 < t/(h/V) < 17.9$. Table 3 indicates close quantitative agreement between

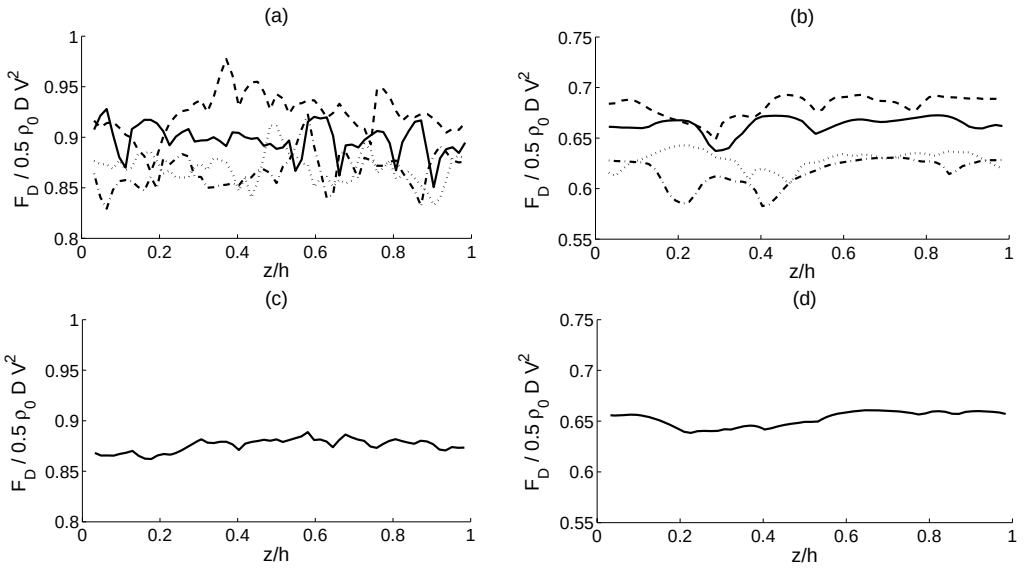

FIGURE 12. Spanwise variation of the drag for $Re = 9,000$, $D/h = 0.1$, $l_c/h = 3$, and $G/h = 0.15$ (a,c) and $G/h = 0.03$ (b,d) at different times during the quasisteady stage: $t/(h/V) = 14.2$ (solid lines), 15.3 (dashed lines), 16.5 (dashed-dotted lines), and 30 (dotted lines). The time-averaged drag is shown in (c) and (d). Notice the spanwise variation of the drag with a characteristic length of about a cylinder diameter D for the larger gap.

parameter	gravity current flow	classic flow
$F_{D,mean}/(0.5\rho_0 DU^2)$	1.25 (1 %)	1.24 [1]
$F_{L,pp}/(0.5\rho_0 DU^2)$	1.11 (13 %)	1.28 [1]
$f/(U/D)$	0.25 (19 %)	0.21 [2]

TABLE 3. Comparison of the mean drag $F_{D,mean}/(0.5\rho_0 DU^2)$, peak-to-peak lift $F_{L,pp}/(0.5\rho_0 DU^2)$, and frequency of the force fluctuations $f/(U/D)$ between the gravity current flow past a circular cylinder far away from the bottom wall at $Re_D = 459$ (3D simulation with $Re = 9,000$, $l_c/h = 3$, and $G/h = 0.15$) and the classic constant density flow past a circular cylinder in infinite domains at $Re_D = 525$ [1] (3D simulation by Mittal & Balachandar (1995)) or $Re_D = 460$ [2] (experiments by Prasad & Williamson (1997)). The relative difference, indicated in per cent, is sufficiently small for constant density flows to provide a useful approximation during the quasisteady stage.

the gravity current flow and the classical case. Hence the interaction between the mixing layer and the Karman vortices, the mean lift component due to buoyancy, and the slight wake deflection towards the bottom wall do not significantly influence the force loading for the present case. We conclude that in this parameter regime the force magnitude and frequency for quasisteady gravity current flows over cylinders can be estimated based on available data from studies of constant density flows past cylinders near walls (Bearman & Zdravkovich (1978); Zdravkovich (1985); Fredsøe & Hansen (1987); Chiew (1991); Lei *et al.* (1999, 2000), among many others).

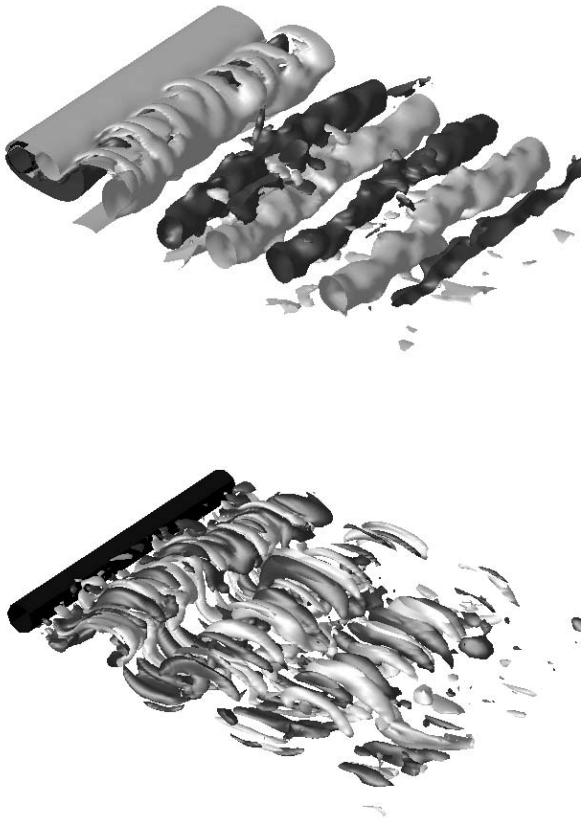

FIGURE 13. Instantaneous spanwise (top) and streamwise (bottom) vorticity isosurfaces ($\omega_z/(V/h) = 4$ and $\omega_x/(V/h) = 4$ in dark grey, and $\omega_z/(V/h) = -4$ and $\omega_x/(V/h) = -4$ in light grey) during the quasisteady stage for $Re = 9,000$, $D/h = 0.1$, $l_c/h = 3$, and $G/h = 0.15$. Notice the presence of primary von Karman vortices and of secondary streamwise vortices in the near wake.

4. Wall shear stress

In the following, we will analyze the dependence of the dimensionless friction velocity u_τ/V on the various flow parameters, due to its importance for the transport of sediment as discussed in section 1. The friction velocity is defined as

$$\frac{u_\tau}{V} = \sqrt{\frac{|\tau_w|}{\rho_0 V^2}} \quad , \quad \frac{|\tau_w|}{\rho_0 V^2} = \frac{1}{Re}\left(\frac{V}{u_b}\right)^{-1}\left[\sqrt{\left(\frac{\partial u/V}{\partial y/h}\right)^2 + \left(\frac{\partial w/V}{\partial y/h}\right)^2}\right]_{y=0} . \qquad (4.1)$$

4.1. *Gravity current flows without obstacles*

For reference purposes, we present data from 2D simulations of gravity current flows without any obstacles. The parameters of these simulations are the same as in section 2.3, but with a grid of $1,200 \times 200$ instead. Figure 16 shows the streamwise variation of the friction velocity for two values of Re at a time when the front of the current is near the end of the domain. Near the front, note the increase of the friction velocity in the upstream direction towards a maximum. This maximum is referred to as $(u_\tau/V)_{head}$. The

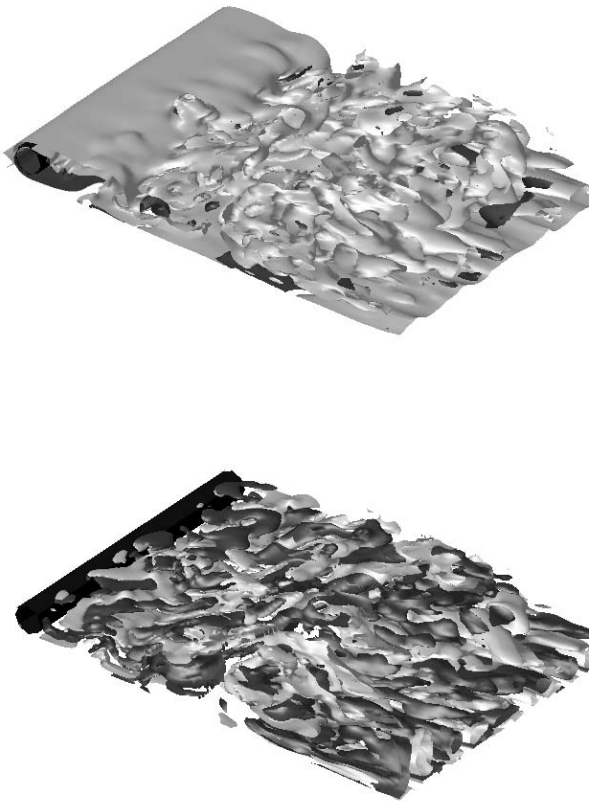

FIGURE 14. Instantaneous spanwise (top) and streamwise (bottom) vorticity isosurfaces ($\omega_z/(V/h) = 4$ and $\omega_x/(V/h) = 4$ in dark grey, and $\omega_z/(V/h) = -4$ and $\omega_x/(V/h) = -4$ in light grey) during the quasisteady stage for $Re = 9,000$, $D/h = 0.1$, $l_c/h = 3$, and $G/h = 0.03$. A comparison with figure 13 indicates that reducing the gap size considerably distorts the flow structures in the near wake.

friction velocity averaged over $-3 < x/h < 2$ is denoted as $(u_\tau/V)_{tail}$. We furthermore define the boundary layer thickness δ_{90}/h during the quasisteady stage as the length over which the horizontal velocity averaged over $-3 < x/h < 2$ increases to 90% of its maximum value.

Figure 17 shows that while V/u_b depends only weakly on Re, the other quantities decrease notably with Re. More importantly, figure 17b shows that the friction velocity at the head of the current is larger than that at the tail. We will employ this information later in the analysis of gravity current flows past cylinders. Also note that the values for $(u_\tau/V)_{head}$ and $(u_\tau/V)_{tail}$ for $H/h = 2.5$ and $l/h = 12$ are close to those for $H/h = 1$ and $l/h \sim 1$ obtained in other studies (Ooi *et al.* (2007*a*); Necker *et al.* (2002); Cantero *et al.* (2008)).

4.2. *Reference case*

Figures 18 and 19 show the temporal evolution of friction velocity for the reference simulation ($Re = 9,000$, $G/h = 0.03$ and $l_c/h = 9$), in which the cylinder is positioned at

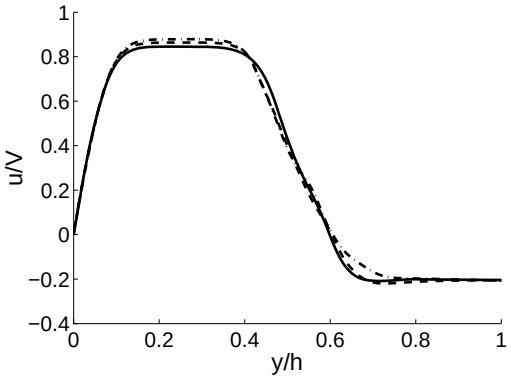

FIGURE 15. Time-averaged horizontal velocity profile upstream of the cylinder during the quasisteady stage ($t/(h/V) = 14.2 - 17.9$) for $Re = 9,000$, $D/h = 0.1$, $l_c/h = 3$, and $G/h = 0.15$ at $z/h = 0.5$ and $x/h = 13.5$ (solid line), 14 (dashed line), and 14.5 (dashed-dotted line). The cylinder is located at $y/h = 0.15 - 0.25$.

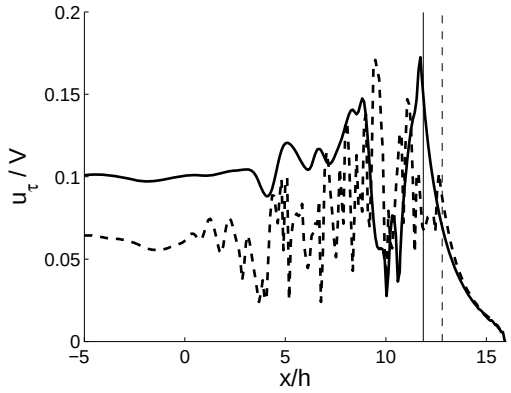

FIGURE 16. Streamwise variation of the friction velocity u_τ/V from 2D simulations of gravity current flows without obstacles, for $H/h = 2.5$ and $Re = 2,000$ (solid line) and $Re = 9,000$ (dashed line). The front of the current is located at $x/h = 11.9$ ($x/h = 12.7$) for $Re = 2,000$ ($Re = 9,000$), and indicated by a vertical solid (dashed) line. Note the larger friction velocities at the head of the current ($x/h \approx 12$), as compared to the tail ($x/h = 0 - 4$).

$x/h = 9 - 9.1$. The maximum friction velocity throughout the entire interaction occurs at $t/(h/V) = 9.3$, shortly after the time of maximum drag ($t/(h/V) = 9.2$), and at $x/h = 9.04$, just upstream of the cylinder's center ($x/h = 9.05$). Large friction velocities are observed near the cylinder during the transient stage, cf. figure 20, especially as the head of the current plunges downward just downstream of the cylinder, cf. figures 3d and 19c. During the quasisteady stage, the friction velocity right below the cylinder is approximately constant with time (figure 20), and about 30% lower than at impact. The fluctuations of the friction velocity immediately downstream of the cylinder ($x/h = 9.1 - 9.5$) in figure 19d result from the shedding of vortices of negative vorticity (figure 3f), as will be discussed below. Similar observations hold for the case of $Re = 45,000$.

Recall from figure 10b that the lobes first make contact with the cylinder at approximately $z/h = 0.16$, 0.42, and 0.77. Figure 21 shows that the friction velocity reaches local maxima at these spanwise positions, which indicates that the lobe and cleft structure governs the spanwise variation of the friction velocity at impact. Similar behavior was observed in the other 3D simulations.

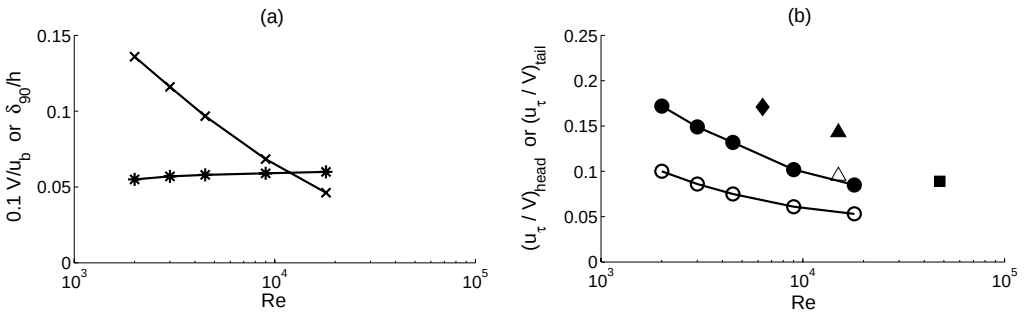

FIGURE 17. Effect of Re on the front speed (V/u_b, asterisks), boundary layer thickness (δ_{90}/h, crosses), friction velocity at the head ($(u_\tau/V)_{head}$, filled circles) and at the tail ($(u_\tau/V)_{tail}$, open circles) from 2D simulations of gravity currents without obstacles for $H/h = 2.5$. Also shown in (b) are results for $(u_\tau/V)_{head}$ (filled symbols) and $(u_\tau/V)_{tail}$ (open symbols) from simulations of gravity currents with $H/h = 1$ and $l/h \sim 1$ by Ooi *et al.* (2007*a*) (square), Necker *et al.* (2002) (diamond), and Cantero *et al.* (2008) (triangles).

4.3. *Range of validity of 2D simulations*

Figures 22 and 23 show that during impact ($t/(h/V) < 3.2$) 2D and 3D simulation data for the spanwise averaged maximum friction velocity agree to within 6%. Of course, spanwise variations of the friction velocity are not captured by 2D simulations. Figure 22 furthermore indicates that during the quasisteady stage ($14.2 < t/(h/V) < 17.7$) the friction velocity tends towards a constant mean value, which is approximately identical in the 2D and 3D simulations. Similarly, figure 23 shows that 2D and 3D simulations give comparable results for the streamwise variation of the friction velocity near the cylinder ($x/h = 2.9 - 3.2$).

For the transient stage ($3.2 < t/(h/V) < 14.2$), figure 22 displays large fluctuations of the friction velocity below the cylinder in both 2D and 3D simulations. Note, however, that this apparently good agreement is due to the short distance between the gate and the cylinder ($l_c/h = 3$), which does not allow for the complete break-up of the Kelvin-Helmholtz vortices in the 3D simulations, as explained earlier. A comparison of figures 20 and 22b indicates significant differences when the 2D simulation is compared with the 3D simulation for $l_c/h = 9$, in which the Kelvin-Helmholtz vortices break up before encountering the cylinder. To conclude, 2D simulations provide accurate information for the friction velocity immediately below the cylinder during the impact stage, and for the time averaged values during the quasisteady stage.

4.4. *Effect of the gap*

Figure 24 displays the effect of the gap size G/h on the streamwise variation of the friction velocity near the cylinder at impact (a) and during the quasisteady stage (b). The maximum friction velocity occurs below the cylinder and decreases for larger gaps.

When vortex shedding is present during the quasisteady stage, it results in friction velocity fluctuations downstream of the cylinder, cf. figure 24b. While the peak of these fluctuations is largest for intermediate gap sizes, we have to keep in mind that 2D simulations generally overpredict the fluctuation amplitudes, cf. figure 23d.

Figure 25 shows the influence of the gap size G/h on the horizontal velocity profile inside the gap, at $x = l_c + D/2$, during impact (a) and during the quasisteady stage (b). We note that the maximum horizontal velocity in the gap remains approximately constant in the range $G/h = 0.03 - 0.075$ ($G/D = 0.3 - 0.75$). This finding is consistent with the open channel flow experiments of Fredsøe & Hansen (1987) and Chiew (1991),

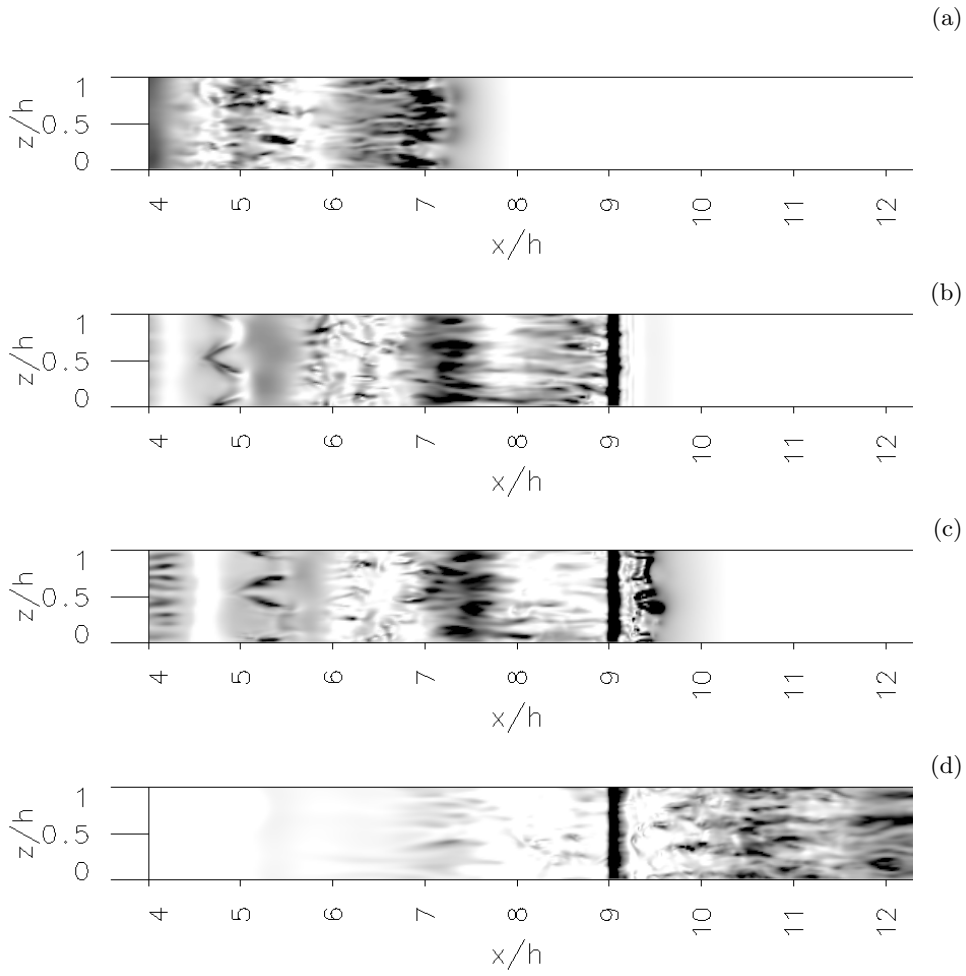

FIGURE 18. Friction velocity contours (u_τ/V) for $Re = 9,000$, $D/h = 0.1$, $l_c/h = 9$ and $G/h = 0.03$ at different times: $t/(h/V) = 7.3$ (a), 9.4 (b, maximum friction velocity below cylinder), 9.9 (c), and 16.5 (d). The cylinder is at $x/h = 9 - 9.1$. Darker shades indicate higher friction velocities.

who observe a small effect of G/D on the average and maximum velocities in the gap for $G/D \geqslant 0.12$.

Since the maximum horizontal velocity in the gap is approximately constant over the range $G/h = 0.03 - 0.075$, it cannot explain the increasing friction velocity for smaller gaps. However, we note in figure 25 a change in the shape of the velocity profile when the gap is increased from $G/h = 0.015$, which suggests a potential transition between different flow regimes. This issue will be further analyzed for a larger set of parameters in section 5.

The streamwise pressure gradient along the bottom wall is directly related to the onset of scour (Sumer & Fredsøe (2002)). Furthermore, since it has to balance the tangential shear stress along the wall, it is also linked to the friction velocity (Panton (1996) p. 338). Note in figure 26 that the streamwise wall pressure gradient $((\partial p/(\rho_0 V^2)) \,/\, (\partial x/h))$ at the cylinder location ($x/h = 3 - 3.1$) decreases for larger gaps. For the present parameter range we can hence attribute the observed decrease of the friction velocity for larger gaps

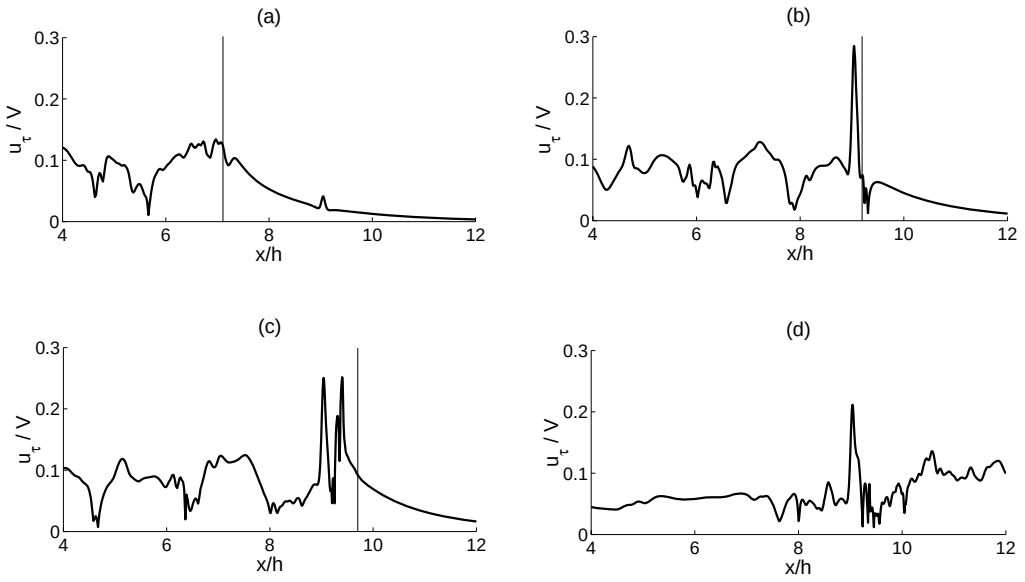

FIGURE 19. Streamwise variation of the friction velocity (u_τ/V) at $z/h = 0.5$ for $Re = 9,000$, $D/h = 0.1$, $l_c/h = 9$ and $G/h = 0.03$ at different times: $t/(h/V) = 7.3$ (a), 9.4 (b, maximum friction velocity below cylinder), 9.9 (c), and 16.5 (d). The cylinder is located at $x/h = 9 - 9.1$. The front of the current using the $c^* = 0.5$ contour at $z/h = 0.5$ is indicated by thin vertical lines. The maximum value of the friction velocity throughout the interaction occurs in (b). Also note the large friction velocities downstream of the cylinder in (c), as the current plunges downstream of the cylinder.

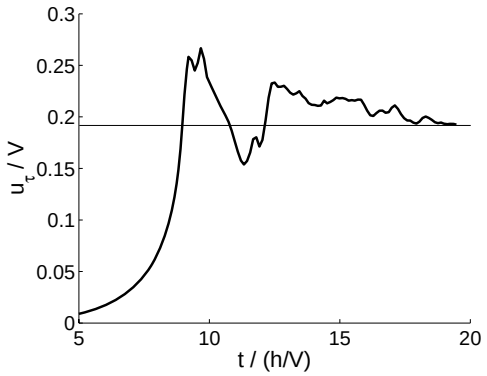

FIGURE 20. Temporal evolution of the spanwise averaged friction velocity u_τ/V immediately below the center of the cylinder $(x = l_c + D/2)$, for $Re = 9,000$, $D/h = 0.1$, $l_c/h = 9$ and $G/h = 0.03$. The horizontal line indicates the quasisteady friction velocity (section 4.6).

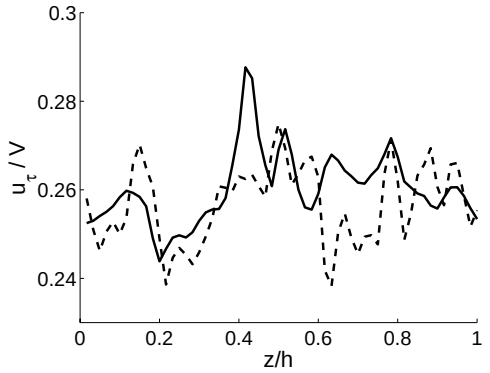

FIGURE 21. Spanwise variation of the friction velocity u_τ/V immediately below the cylinder center at $x = l_c + D/2$, for $Re = 9,000$, $D/h = 0.1$, $l_c/h = 9$ and $G/h = 0.03$ at $t/(h/V) = 9.2$ (solid line) and 9.3 (dashed line).

to a decrease of the streamwise pressure gradient, which is directly influenced when the cylinder is moved away from the bottom wall.

Figure 27 shows the spanwise peak-to-peak variation of the friction velocity during impact. Values up to $0.04V$ (15%) and $0.09V$ (50%) are reached for $G/h = 0.03$ and $G/h = 0.15$, respectively. Interestingly, while the friction velocity is lower for larger gaps,

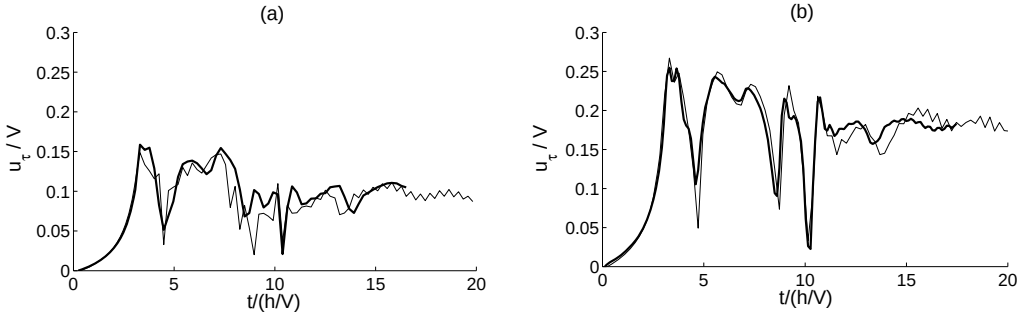

FIGURE 22. Comparison of the spanwise averaged friction velocity u_τ/V immediately below the cylinder: 2D (thin lines) and 3D (thick lines) simulations for $Re = 9,000$, $D/h = 0.1$, $l_c/h = 3$, and $G/h = 0.15$ (a) and $G/h = 0.03$ (b).

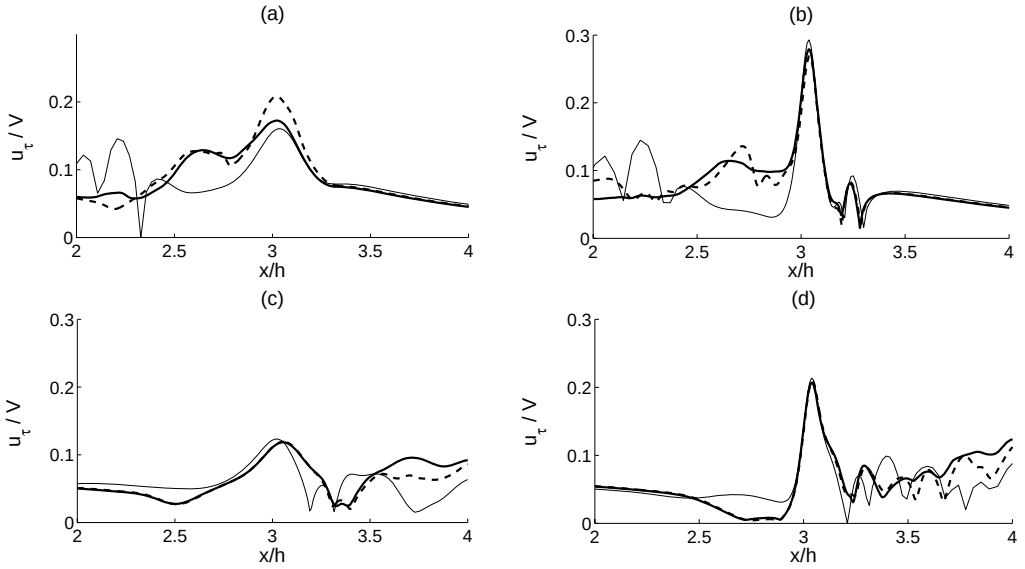

FIGURE 23. Comparison of the streamwise variation of the friction velocity u_τ/V near the cylinder: 2D (thin lines) and 3D (thick lines) simulations for $Re = 9,000$, $D/h = 0.1$, $l_c/h = 3$ and $G/h = 0.15$ (a,c) and $G/h = 0.03$ (b,d). Times are $t/(h/V) = 3.3$ (a,b) and $t/(h/V) = 15.3$ (c,d). In frames (a,b) the current front is located at $x/h \approx 3.2$, while in frames (c,d) it has reached $x/h \approx 14.4$. Both the spanwise-averaged (solid lines) and the $z/h = 0.5$ (dashed lines) values of u_τ/V are shown from the 3D simulations. The cylinder is located at $x/h = 3 - 3.1$.

its spanwise variation is more pronounced. As discussed earlier for the reference case, the spanwise variation of the friction velocity at impact is governed by the lobe and cleft structure. During the quasisteady stage, the spanwise variations are minimal.

4.5. *Effect of the Reynolds number*

For $G/h = 0.03$, figure 28 shows that the maximum friction velocity below the cylinder decreases with increasing Re. This is expected, since from definition (4.1) $u_\tau/V \to 0$ as $Re \to \infty$. In addition, we found (not shown) that as we increase Re from 2,000 to 18,000 for $G/h = 0.03$, the horizontal velocities in the gap increase, while the pressure gradient below the cylinder remains approximately constant. The implications of this for u_τ/V will be further discussed in section 5 for a larger set of parameters. Re has a

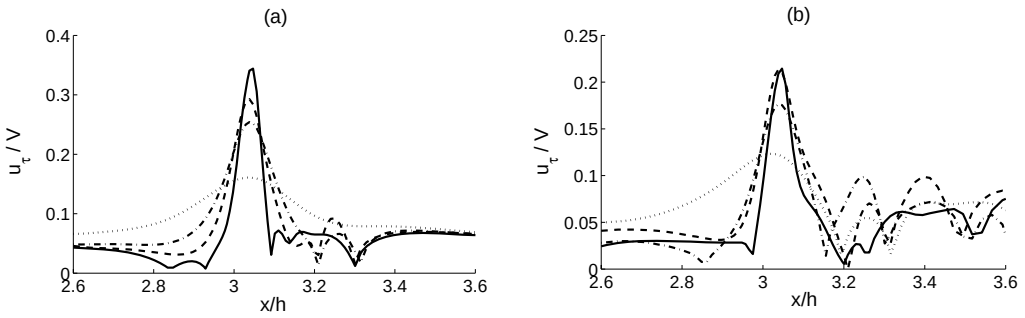

FIGURE 24. Effect of G/h on the streamwise variation of the friction velocity u_τ/V near the cylinder at impact (a, $t/(h/V) = 3.3$) and during the quasisteady stage (b, $t/(h/V) = 15.3$). 2D simulations for $Re = 9,000$, $D/h = 0.1$, $l_c/h = 3$ and different values of G/h: 0.015 (solid line), 0.03 (dashed line), 0.05 (dashed-dotted line) and 0.15 (dotted line). The cylinder is located at $x/h = 3 - 3.1$. The maximum friction velocity occurs below the cylinder and decreases for larger gaps.

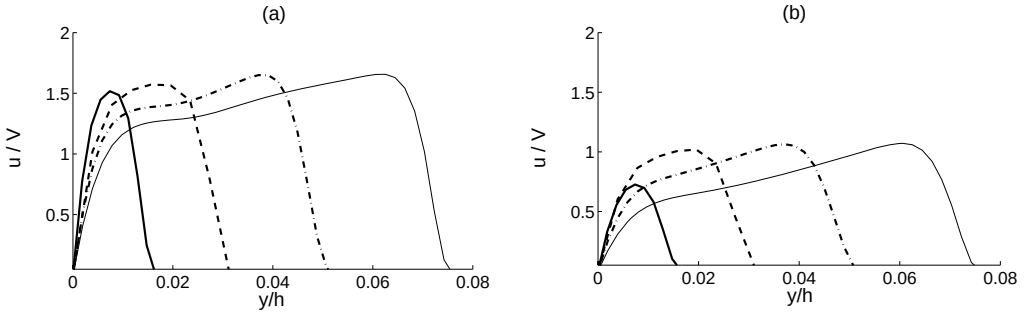

FIGURE 25. Effect of G/h on the horizontal velocity profile within the gap at impact (a, $t/(h/V) = 3.3$) and during the quasisteady stage (b, $t/(h/V) = 15.3$). 2D simulations for $Re = 9,000$, $D/h = 0.1$, $l_c/h = 3$ and different values of G/h: 0.015 (thick solid line), 0.03 (dashed line), 0.05 (dashed-dotted line), and 0.075 (thin solid line).

similar influence on the spanwise variations of drag and friction velocity at impact: the characteristic length scale of these variations decreases as Re increases, due to smaller lobes.

4.6. *Dominant parameters*

We will now attempt to quantify the dependence of the friction velocity below the cylinder on the dominant parameters of the problem. Towards this end, we take as the representative friction velocity during the impact stage the maximum value in the intervals $2.95 < x/h < 3.15$ and $2.8 < t/(h/V) < 3.8$. As representative quasisteady friction velocity, we take the time-averaged value at $x/h = 3.05$.

The friction velocity u_τ below the cylinder depends on

$$u_\tau = f\left(G, D, \delta_{90}, V, \nu\right) \ . \tag{4.2}$$

The lock height h is not included among the list of parameters, since in practice gravity current heights of $h/2$ (Simpson (1997); Shin *et al.* (2004)) are much larger than D and G, as discussed in section 2.3. We note that if V were not included, then h would enter the dependency through $\sqrt{g'h}$. By taking G and V as the repeating variables in the above

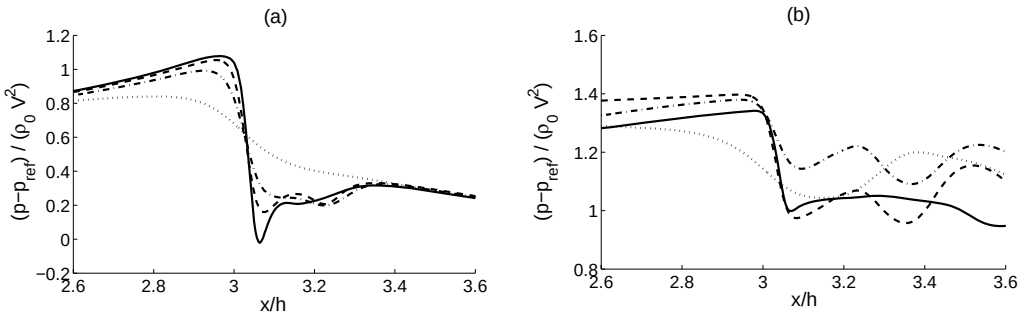

FIGURE 26. Effect of G/h on the streamwise variation of the pressure $((p - p_{ref})/(\rho_0 V^2))$ at the bottom wall near the cylinder: impact (a, $t/(h/V) = 3.3$) and quasisteady stage (b, $t/(h/V) = 15.3$. The data are from 2D simulations for $Re = 9,000$, $D/h = 0.1$, $l_c/h = 3$ and different values of G/h: 0.015 (solid line), 0.03 (dashed line), 0.05 (dashed-dotted line), and 0.15 (dotted line). The cylinder is located at $x/h = 3 - 3.1$. The streamwise pressure gradient decreases for larger gaps.

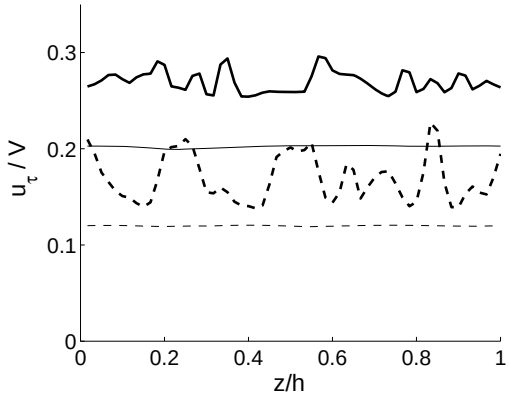

FIGURE 27. Effect of G/h on the spanwise variation of the friction velocity u_τ/V below the cylinder at impact (thick lines, $t/(h/V) = 3.3$) and during the quasisteady stage (thin lines, $t/(h/V) = 15.3$). The data are from 3D simulations for $Re = 9,000$, $D/h = 0.1$, $l_c/h = 3$ and different values of G/h: 0.03 (solid lines) and 0.15 (dashed lines). While the mean friction velocity is lower for larger gaps, its spanwise variation is more pronounced.

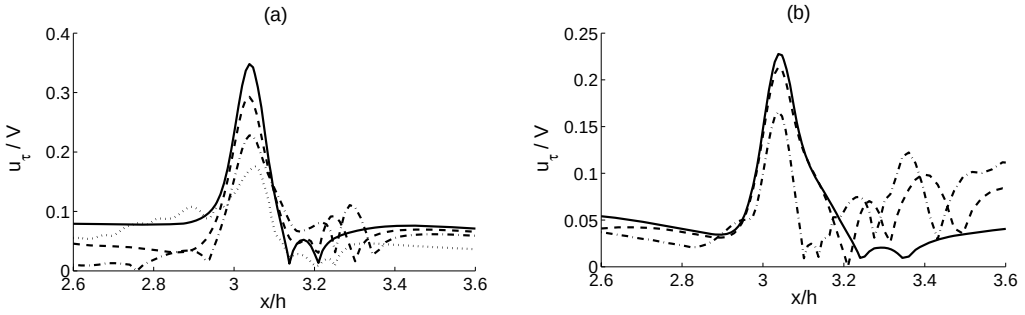

FIGURE 28. Effect of Re on the streamwise variation of the friction velocity u_τ/V near the cylinder at impact (a, $t/(h/V) = 3.3$) and during the quasisteady stage (b, $t/(h/V) = 15.3$). Data are from 2D simulations for $D/h = 0.1$, $G/h = 0.03$, $l_c/h = 3$ and different values of Re: 4,500 (solid line), 9,000 (dashed line), and 18,000 (dashed-dotted line). The dotted line in (a) shows the friction velocity at $z/h = 0.5$ from the 3D simulation with $Re = 45,000$. The cylinder is located at $x/h = 3 - 3.1$.

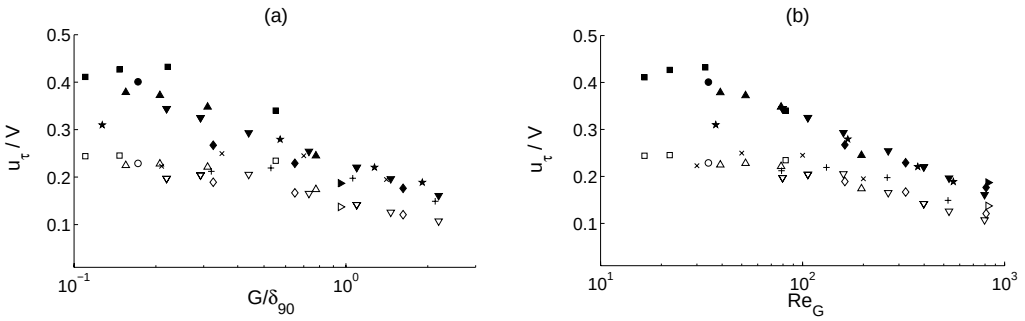

FIGURE 29. Effect of G/δ_{90} (a) and Re_G (b) on the maximum (closed symbols) and quasisteady (open symbols) friction velocity u_τ/V for $H/h = 2.5$, $D/h = 0.1$, $l_c/h = 3$, and different values of G/h and Re. The different values of Re are denoted as follows: Re =2,000 (squares), 3,000 (circles), 4,500 (triangles), 9,000 (inverted triangles), 18,000 (diamonds), and 45,000 (right triangle). Results from simulations for larger cylinders with $D/h = 0.15$, $H/h = 5$ and $Re = 6,000$ are also shown (stars). Data from 2D simulations of constant density boundary layer flows past a circular cylinder near a bottom wall at $Re_D = 200$ (crosses) and $Re_D = 525$ (plus signs) are indicated for comparison.

dependency, Buckingham's Π-theorem gives

$$\frac{u_\tau}{V} = F\left(\frac{G}{D}, \frac{G}{\delta_{90}}, Re_G\right) , \tag{4.3}$$

where Re_G is a gap Reynolds number defined as $Re_G = VG/\nu$. However, the parameters we control directly in the simulations are G/h, Re, and D/h, so that we can modify the values of the parameters in the above relation only indirectly. G/D is varied by changing G/h in the range $G/h = 0.015-0.15$, and by employing both $D/h = 0.1$ and $D/h = 0.15$. G/δ_{90} is varied through G/h and Re, which is related to δ_{90}/h as shown in figure 17a. Here Re is changed in the range $Re = 2,000 - 45,000$. Finally, the gap Reynolds number Re_G is varied by changing G/h and Re, since $Re_G = Re(G/h)(V/u_b)$.

While we observed an overall decrease of the maximum and quasisteady friction velocities for increasing G/D, there was substantial scatter in the data when we graphed them against G/D. On the other hand, we obtained better collapse when plotting the data against G/δ_{90} and Re_G. The dependence of the maximum and quasisteady friction velocities on these parameters is shown in figure 29. Note the particularly good collapse of the data as function of Re_G.

5. Implications for scour

We now discuss the effect of the cylinder presence on the friction velocity. Compared to a flow without obstacles, the cylinder presence produces a steep pressure gradient at the bottom wall, which increases the friction velocity immediately below the cylinder, due to the balance between the pressure gradient and the tangential shear stress at a no-slip wall (Panton (1996) p. 338). Hence it is useful to analyze the ratio of the friction velocities with and without the cylinder, which in scour studies commonly is referred to as the amplification factor AF (Sumer & Fredsøe (2002)). We define the impact amplification factor as the ratio of the maximum friction velocity immediately below the cylinder to the friction velocity at the head of a current without cylinder, cf. section 4.1. A corresponding definition is employed for the quasisteady amplification factor.

Figure 30 shows that AF increases with Re_G for $Re_G \lesssim O(100)$, while it decreases for

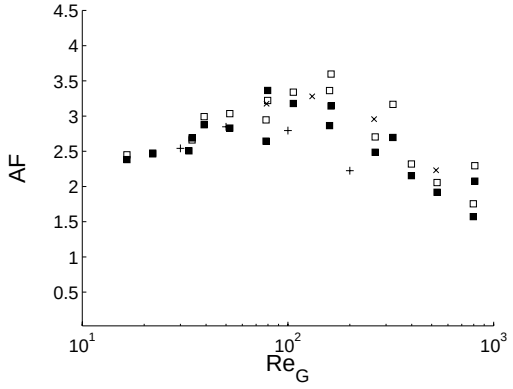

FIGURE 30. Effect of Re_G on the impact (filled squares) and quasisteady (open squares) values of the amplification factor (AF) for $H/h = 2.5$, $D/h = 0.1$, $l_c/h = 3$, and different values of G/h and Re. Also shown are results from 2D simulations of constant density boundary layer flows past a circular cylinder near a bottom wall at $Re_D = 200$ (crosses) and $Re_D = 525$ (plus signs). The impact amplification factor is comparable to the quasisteady value.

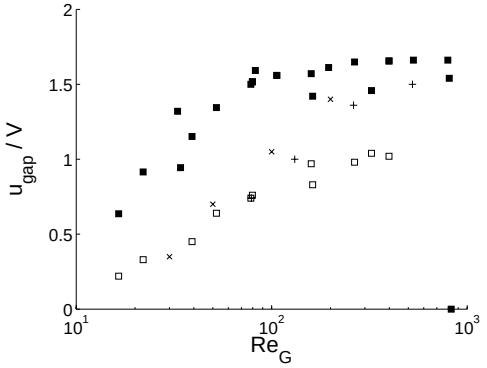

FIGURE 31. Effect of Re_G on the maximum velocity in the gap during the impact (filled squares, $t/(h/V) = 3.3$) and quasisteady (open squares) stages. Simulation parameters are $H/h = 2.5$, $D/h = 0.1$, $l_c/h = 3$, and different values of G/h and Re. Data from 2D simulations of constant density boundary layer flows past a circular cylinder near a bottom wall at $Re_D = 200$ (crosses) and $Re_D = 525$ (plus signs) are indicated for comparison.

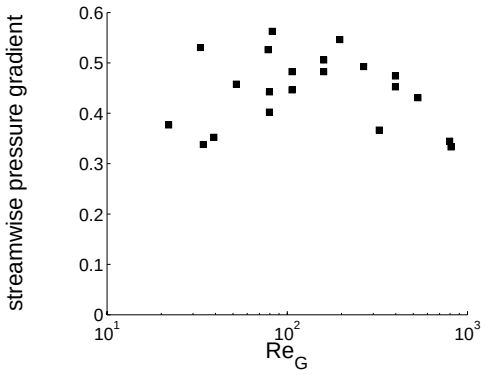

FIGURE 32. Influence of Re_G on the magnitude of the streamwise pressure gradient below the cylinder $\left|(\partial p/(\rho_0 V^2)) \,/\, (\partial x/G)\right|$ during impact ($t/(h/V) = 3.3$). Simulation parameters are $H/h = 2.5$, $D/h = 0.1$, $l_c/h = 3$, and different values of G/h and Re.

higher Re_G. For $Re_G \lesssim O(100)$, as Re_G increases more of the faster moving fluid away from the wall enters inside the gap, cf. figure 31. This increases the pressure gradient $\left|(\partial p/(\rho_0 V^2)) \,/\, (\partial x/G)\right|$ below the cylinder, cf. figure 32, so that AF increases. In figure 31, u_{gap}/V is the maximum horizontal velocity at $x/h = 3.05$, and its value at $t/(h/V) = 3.3$ is employed to characterize the impact stage, while a temporally averaged value is used for the quasisteady stage. On the other hand, notice in figure 31 that the velocities inside the gap stay approximately constant for $Re_G \gtrsim O(100)$. When $Re_G \gtrsim O(100)$, as Re_G increases, the pressure gradient $\left|(\partial p/(\rho_0 V^2)) \,/\, (\partial x/G)\right|$ produced by the presence of the cylinder decreases, cf. figure 32, resulting in a decrease of AF.

Figure 30 also shows that the amplification factor during impact is about the same as during the quasisteady stage. In other words, the presence of the cylinder amplifies the friction velocity of a current without obstacle proportionally during all stages of the interaction. The largest friction velocities occur at the head of the current as they balance the strong horizontal pressure gradient there (Benjamin (1968); Panton (1996)).

We can now compare the above results to those from 2D simulations of constant density boundary layer flows past circular cylinders near walls at $Re_D = UD/\nu$ of 200 and 525, where U is the horizontal velocity outside the boundary layer. The gap G/D is varied in the range $G/D = 0.15 - 1.5$. The complete parameters of these 2D simulations can be found in Gonzalez-Juez (2009). We find that for gravity currents and constant density flows, Re_G has a similar effect on the friction velocity below the cylinder (figure 29b), on the amplification factor (figure 30), and on the maximum horizontal velocity in the gap (figure 31). (Note that V denotes the front velocity for the gravity current, and the free stream velocity for the constant density flow.) Hence, if we know the friction velocities at the head and tail of a gravity current without obstacle (section 4.1), we can employ the amplification factor for constant density flows past cylinders near walls to estimate the friction velocity for gravity currents in the presence of a cylinder.

We now discuss the onset of scour near a pipe embedded in an erodible bed of uniform and cohesionless sediment. Scour starts when the difference in pressure upstream and downstream of the pipe Δp, which induces a seepage flow beneath the pipe, is sufficiently large to break the soil under the pipe, a process that is referred to as piping. A necessary condition for this break to occur is (Chiew (1990); Sumer *et al.* (2001))

$$\frac{\Delta p/(\rho_0 g)}{\Delta x} \geqslant i_f \ . \tag{5.1}$$

Here Δx is the streamwise distance across which the pressure difference is established, and i_f denotes a property of the bed called the floatation gradient. The pressure gradient $\Delta p/(\rho_0 g)/\Delta x$ can be either dynamic or static (Chiew (1990); Sumer *et al.* (2001)). A further necessary condition is that $\Delta p/(\rho_0 g)/\Delta x$ must be maintained for a sufficiently long time, or, if cyclic and with a short time period, $\Delta p/(\rho_0 g)/\Delta x$ should occur repeatedly (Sumer *et al.* (2001)). Past studies have addressed the onset of scour in both steady and wavy flows (e.g. Mao (1986); Chiew (1990); Sumer *et al.* (2001)).

The pressure difference $\Delta p/(\rho_0 g)/\Delta x$ for bottom-mounted square cylinders in gravity current flows can now be estimated, along with the time interval over which this pressure difference is maintained. Towards this end, we will make partial use of the results obtained by Gonzalez-Juez *et al.* (2008). Consider a gravity current of height $h/2$ about to encounter a bottom-mounted square cylinder of side D, cf. figure 33, under the realistic conditions of $h \ll H$ and $D \ll h$. The hydrostatic pressure at $y = 0$ (the sediment bed surface) immediately upstream of the cylinder can be estimated as $\rho_0 g(H - h/2) + \rho_1 g h/2$, while its counterpart immediately downstream of the cylinder is $\rho_0 g H$. The dynamic pressure is estimated as $0.5\rho_0 V^2$ upstream of the cylinder, and zero downstream, since the wake is very weak at impact (Gonzalez-Juez *et al.* (2008)). For an inviscid gravity current with $h \ll H$, Shin *et al.* (2004) predict a front speed of $V = \sqrt{g'h/2}$. Thus, by taking $\Delta x = D$, we obtain

$$\frac{\Delta p/(\rho_0 g)}{\Delta x} = 0.75 \left(\frac{D}{h}\right)^{-1} \left(\frac{\Delta \rho}{\rho_0}\right) \ . \tag{5.2}$$

Because the flow is essentially inviscid ($Re \to \infty$), equation (5.2) is applicable to full-scale flows. By combining equations (5.1) and (5.2), we obtain the following preliminary

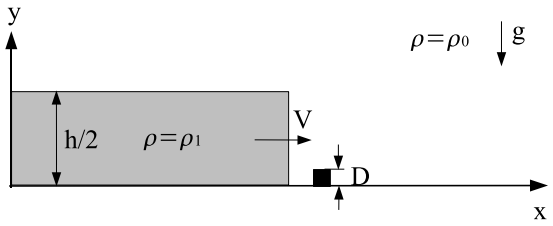

FIGURE 33. Gravity current of height $h/2$ about to encounter a bottom-mounted square cylinder of side D.

criterion for the onset of scour when a gravity current encounters a submerged cylinder

$$0.75 \left(\frac{D}{h}\right)^{-1} \left(\frac{\Delta\rho}{\rho_0}\right) \geqslant i_f \ . \tag{5.3}$$

Typical submarine applications may involve parameter values $D/h \approx 0.005 - 0.5$, cf. section 2.3, and $\Delta\rho/\rho_0 \lesssim 0.05$. We can assume $i_f \approx 1$, based on the values of 0.9 and 0.77 determined experimentally by Chiew (1990) and Sumer *et al.* (2001), respectively. We conclude that it is possible for the inequality (5.3) to be satisfied by typical Boussinesq gravity currents, so that piping may occur.

It remains to be shown that the pressure difference given by equation (5.2) can be sustained for sufficiently long times. Towards this end, we assume that the time interval during which this pressure difference is sustained Δt scales with the time D/V it takes for the gravity current to advance one cylinder diameter. With $V = \sqrt{g'h/2}$ we obtain $D/V = \sqrt{2D^2/(g'h)}$. Typical gravity current heights $h/2$ are $10 - 100\ m$ in the ocean (Kneller *et al.* (1999)), and $0.05 - 0.5\ m$ in the laboratory. We take a characteristic cylinder diameter of $1\ m$ for ocean conditions, and $0.01\ m$ for laboratory conditions, and a density difference of $\Delta\rho/\rho_0 \approx 0.01$. Thus, we obtain $\Delta t \sim 1\ s$ for ocean conditions, and $\Delta t \sim 0.1\ s$ for laboratory conditions. Since Sumer *et al.* (2001) reports that a time interval of $5\ s$ suffices for piping to occur under the conditions of their experiments, while $0.5\ s$ does not, our estimates for the time interval over which $\Delta p/(\rho_0 g)/\Delta x$ is maintained suggest that piping may occur in the ocean, while it will probably not occur in the laboratory.

We conclude that a sufficiently large pressure difference may be maintained over a long enough time interval for piping to occur in the ocean. We also note that the lobe and cleft structure may well cause substantial spanwise variations of this pressure difference, cf. section 3.4, so that scouring may be initiated locally (Sumer & Fredsøe (2002)).

6. Summary and conclusions

The present investigation focuses on the flow of compositional gravity currents past circular cylinders mounted above a non-erodible wall. It employs Navier-Stokes simulations to quantify the force load on the cylinder, along with the friction velocity at the bottom wall near the cylinder. The simulation results are then analyzed with a view towards the occurrence of scour near pipelines mounted on erodible beds. In order to address practically relevant situations, we consider a sufficiently large ratio of the channel height and the lock height ($H/h = 2.5$), and a small ratio of the cylinder diameter and the lock height ($D/h = 0.1$). The Reynolds numbers in the range of $2,000 - 45,000$ are typical for laboratory scale flows.

Comparisons of 2D and 3D simulations show that 2D simulations accurately capture

the overall features of the impact stage. Clearly, 3D simulations are required to reproduce the spanwise variations caused by the lobe and cleft structure. Throughout the transient stage, 2D simulations notably overpredict the fluctuations of the force load and friction velocity, due to unphysically coherent Kelvin-Helmholtz billows. During the quasisteady stage, 2D simulations give accurate results for the spanwise and temporally averaged friction velocity below the cylinder, as long as there are no separated flow regions propagating along the bottom wall. These findings support previous results from 2D simulations by Gonzalez-Juez *et al.* (2009).

Comparisons between gravity current and constant density flows past circular cylinders show that the impact and transient stages are unique to gravity current flows. On the other hand, there are strong similarities between the two during the quasisteady stage: Specifically, the wake structures are similar, and the values of the drag, peak-to-peak lift, vortex shedding frequency, and friction velocity below the cylinder are comparable. Consequently, the values of these quantities during the quasisteady stage of a gravity current flow can be estimated to within $10-20\%$ (for the parameters considered here) using existing data for the well-studied constant density flow past a circular cylinder near a wall.

The mechanisms governing the dynamics of the flow in the gap are discussed, and it is shown that the friction velocity below the cylinder depends chiefly on the Reynolds number Re_G formed with the front velocity and the gap width. The maximum friction velocity at impact is about 1.6 times larger than during the quasisteady stage, or in constant density flows. Hence aggressive tunneling erosion can occur at impact, which represents a key difference between the scour dynamics of gravity current and constant density flows. Furthermore, the larger friction velocity near the lobes (by about 15%) may trigger localized scour. During the quasisteady stage, as a result of vortex shedding for sufficiently large gaps, lee wake erosion may occur. We note that the above comments are based on friction velocity data obtained from simulations for non-erodible beds. Clearly, future research should extend the scope of the simulations to erodible boundaries, and it should involve comparisons with corresponding laboratory experiments.

Acknowledgment

The authors wish to acknowledge several helpful discussions with Prof. Stephen McLean. E. G.-J. is being supported by National Science Foundation IGERT grant DGE02-21715, as well as by a Cota-Robles fellowship. Computing time has been provided by the California NanoSystems Institute at UC Santa-Barbara and Hewlett-Packard, and by the National Center for High Performance Computing in Taiwan.

REFERENCES

Bearman, P. W. & Zdravkovich, M. M. 1978 Flow around a circular cylinder near a plane boundary. *J. Fluid Mech.* **89**, 33–47.

Benjamin, T. B. 1968 Gravity currents and related phenomena. *J. Fluid Mech.* **31**, 209–248.

Bruschi, R., Bughi, S., Spinazze, M., Torselletti, E. & Vitali, L. 2006 Impact of debris flows and turbidity currents on seafloor structures. *Norw. J. Geol.* **86**, 317–337.

Cantero, M., Balachandar, S., Garcia, M. & Bock, D. 2008 Turbulent structures in planar gravity currents and their influence on the flow dynamics. *J. Geophys. Res. - Oceans* **113**.

Cantero, M. I., Lee, J. R., Balachandar, S. & Garcia, M. H. 2007 On the front velocity of gravity currents. *J. Fluid Mech.* **586**, 1–39.

Chang, K. S., Constantinescu, G. & Park, S.-O. 2006 Analysis of the flow and mass

transfer processes for the incompressible flow past an open cavity with a laminar and a fully turbulent incoming boundary layer. *J. Fluid Mech.* **561**, 113–145.

Chang, K. S., Constantinescu, G. & Park, S.-O. 2007*a* The purging of a neutrally buoyant or a dense miscible contaminant from a rectangular cavity. Part I: The case of an incoming laminar boundary layer. *J. Hyd. Eng.* **133**, 361–372.

Chang, K. S., Constantinescu, G. & Park, S.-O. 2007*b* The purging of a neutrally buoyant or a dense miscible contaminant from a rectangular cavity. Part II: The case of an incoming fully turbulent overflow. *J. Hyd. Eng.* **133**, 373–385.

Chiew, Y. 1991 Flow Around Horizontal Circular Cylinder in Shallow Flows. *J. Waterw. Port. Coastal Ocean Eng.* **117** (2), 120–135.

Chiew, Y. M. 1990 Mechanics of local scour around submarine pipelines. *J. Hyd. Eng.* **116** (4), 515–529.

Dengler, A. T. & Wilde, P. 1987 Turbidity currents on steep slopes: Application of an avalanche-type numeric model for ocean thermal energy conversion design. *Ocean Eng.* **14**, 409–433.

Ermanyuk, E. V. & Gavrilov, N. V. 2005*a* Interaction of an internal gravity current with a submerged circular cylinder. *J. Appl. Mech. Tech. Phys.* **46** (2), 216–223.

Ermanyuk, E. V. & Gavrilov, N. V. 2005*b* Interaction of an internal gravity current with an obstacle on the channel bottom. *J. Appl. Mech. Tech. Phys.* **46** (4), 489–495.

Fredsøe, J. & Hansen, E. A. 1987 Lift Forces on Pipelines in Steady Flow. *J. Waterw. Port. Coastal Ocean Eng.* **113** (2), 139–155.

Germano, M., Piomelli, U., Moin, P. & Cabot, W. H. 1991 A dynamic subgrid-scale eddy viscosity model. *Phys. Fluids* **3** (7), 1760–1765.

Gonzalez-Juez, E. D. 2009 Gravity current - submarine structure interaction: Hazard analysis via high-resolution simulations. PhD thesis, University of California at Santa Barbara.

Gonzalez-Juez, E. D., Constantinescu, S. G. & Meiburg, E. 2007 A study of the interaction of a gravity current with a square cylinder using two-dimensional numerical simulations. In *Proceedings of the 26th International Conference on Offshore Mechanics and Arctic Engineering*.

Gonzalez-Juez, E. D. & Meiburg, E. 2009 Shallow water analysis of gravity current flows past isolated obstacles. Submitted to J. Fluid Mech.

Gonzalez-Juez, E. D., Meiburg, E. & Constantinescu, S. G. 2008 Gravity currents impinging on submerged cylinders: Flow fields and associated forces. Accepted for publication in J. Fluid Mech.

Gonzalez-Juez, E. D., Meiburg, E. & Constantinescu, S. G. 2009 The interaction of a gravity current with a circular cylinder mounted above a wall: Effect of the gap size. Accepted for publication in J. Fluid Struct.

Graf, W. H. 1984 *Hydraulics of Sediment Transport*. Published by Water Resources Publication.

Härtel, C., Carlsson, F. & Thunblom, M. 2000*a* Analysis and direct numerical simulation of the flow at a gravity-current head. Part 2. The lobe-and-cleft instability. *J. Fluid Mech.* **418**, 213–229.

Härtel, C., Meiburg, E. & Necker, F. 2000*b* Analysis and direct numerical simulation of the flow at a gravity-current head. Part 1. Flow topology and front speed for slip and no-slip boundaries. *J. Fluid Mech.* **418**, 189–212.

Kneller, B., Bennett, S. J. & McCaffrey, W. D. 1999 Velocity structure, turbulence and fluid stresses in experimental gravity currents. *J. Geophys. Res. - Oceans* **104** (C3), 5381–5391.

Lei, C., Cheng, L., Armfield, S. W. & Kavanagh, K. 2000 Vortex shedding suppression for flow over a circular cylinder near a plane boundary. *Ocean Eng.* **27** (10), 1109–1127.

Lei, C., Cheng, L. & Kavanagh, K. 1999 Re-examination of the effect of a plane boundary on force and vortex shedding of a circular cylinder. *J. Wind Eng. Ind. Aero.* **80** (3), 263–286.

Lilly, D. K. 1992 A proposed modification of the germano-subgrid-scale closure method. *Phys. Fluids* **4** (3), 633–635.

Mao, Y. 1986 The interaction between a pipeline and an erodible bed. PhD thesis, Institute of Hydrodynamics and Hydraulic Engineering, Technical University of Denmark.

Martinuzzi, R. & Tropea, C. 1993 The flow around surface-mounted, prismatic obstacles placed in a fully developed channel flow. *J. Fluids Eng.* **115** (1), 85–92.

Meiburg, E. & Kneller, B. 2009 Turbidity currents and their deposits. Submitted to Ann. Rev. Fluid Mech.

Middleton, G. V. 1993 Sediment Deposition from Turbidity Currents. *Annu. Rev. Earth Planet. Sci.* **21** (1), 89–114.

Mittal, R. & Balachandar, S. 1995 Effect of three-dimensionality on the lift and drag of nominally two-dimensional cylinders. *Phys. Fluids* **7** (8), 1841–1865.

Necker, F., Hartel, C., Kleiser, L. & Meiburg, E. 2002 High-resolution simulations of particle-driven gravity currents. *Int. J. Multiphase Flow* **28** (2), 279–300.

Niedoroda, A. W., Reed, C. W., Parsons, B. S., Breza, J., Forristall, G. Z. & Mullee, J. E. 2000 Developing engineering design criteria for mass gravity flows in deepsea slope environments. In *Proceedings of the Offshore Technology Conference*.

Ooi, S. K., Constantinescu, S. G. & Weber, L. 2005 Two-dimensional large eddy simulation of lock-exchange gravity current flows. In *Proceedings of the 31st International Association Hydraulic Research Congress*.

Ooi, S. K., Constantinescu, S. G. & Weber, L. 2007*a* Numerical simulations of lock-exchange compositional gravity currents. Submitted to J. Fluid Mech.

Ooi, S. K., Constantinescu, S. G. & Weber, L. 2007*b* A numerical study of intrusive compositional gravity currents. *Phys. Fluids* **19**.

Ooi, S. K., Constantinescu, S. G. & Weber, L. 2007*c* Two-dimensional large-eddy simulation of lock-exchange gravity current flows at high grashof numbers. *J. Hyd. Eng.* **133** (9), 1037–1047.

Panton, R. L. 1996 *Incompressible Flow*. John Wiley and Sons.

Pierce, C. D. 2001 Progress-variable approach for large eddy simulation of turbulent combustion. PhD thesis, Stanford University.

Pierce, C. D. & Moin, P. 2004 Progress-variable approach for large-eddy simulation of non-premixed turbulent combustion. *J. Fluid Mech.* **504**, 73–97.

Prasad, A. & Williamson, C. H. K. 1997 Three-dimensional effects in turbulent bluff-body wakes. *J. of Fluid Mech.* **343**, 235–265.

Ross, S. L., Boore, D. M., Fisher, M. A., Frankel, A. D., Geist, E. L., Hudnut, K. W., Kayen, R. E., Lee, H. J., Normark, W. R. & Wong, F. L. 2004 Comments on potential geologic and seismic hazards affecting coastal ventura county, california. *Open-File Report 2004-1286 from the U.S. Geological Survey* .

Shin, J. O., Dalziel, S. B. & Linden, P. F. 2004 Gravity currents produced by lock exchange. *J. Fluid Mech.* **521**, 1–34.

Simpson, J. E. 1972 Effects of the lower boundary on the head of a gravity current. *J. Fluid Mech.* **53**, 759–768.

Simpson, J. E. 1997 *Gravity Currents in the Environment and the Laboratory*. Cambridge University Press.

Sumer, B. M. & Fredsøe, J. 2002 *The Mechanics of Scour in the Marine Environment*. World Scientific.

Sumer, B. M., Truelsen, C., Sichmann, T. & Fredsøe, J. 2001 Onset of scour below pipelines and self-burial. *Coast. Eng.* **42** (4), 313–335.

Taniguchi, S. & Miyakoshi, K. 1990 Fluctuating fluid forces acting on a circular cylinder and interference with a plane wall. *Exps. in Fluids* **9** (4), 197–204.

Thomas, L. P., Dalziel, S. B. & Marino, B. M. 2003 The structure of the head of an inertial gravity current determined by particle-tracking velocimetry. *Exps. Fluids* **34** (6), 708–716.

Whitehouse, R. 1998 *Scour at Marine Structures: A Manual for Practical Applications*. Thomas Telford.

Williamson, C. H. K. 1996 Vortex dynamics in the cylinder wake. *Ann. Rev. Fluid Mech.* **28**, 477–539.

Zdravkovich, M. M. 1985 Forces on a circular cylinder near a plane boundary. *Appl. Ocean Res.* **7** (4), 197–201.

Zdravkovich, M. M. 1997 *Flow Around Circular Cylinders Vol. 1: Fundamentals*. Oxford University Press.